(2)

AD

US ARMY
LABORATORY COMMAND
MATERIALS TECHNOLOGY LABORATORY

MTL TR 92-24

SINGLE CRYSTAL GROWTH OPTIMIZATION OF MAGNESIUM-DOPED LITHIUM NIOBATE

April 1992

R. G. SCHLECHT, C. I. ZANELLI, and A. M. SCHLECHT
LaserGenics Corporation
2362 Qume Drive, Suite E
San Jose, CA 95131

P. F. BORDUI, C. D. BIRD, and R. BLACHMAN
Crystal Technology, Incorporated
1040 East Meadow Circle
Palo Alto, CA 94303

FINAL REPORT

Contract DAAL04-88-C-0029

Approved for public release; distribution unlimited.

Prepared for

U.S. ARMY MATERIALS TECHNOLOGY LABORATORY
Watertown, Massachusetts 02172-0001

REPORT DOCUMENTATION PAGE

READ INSTRUCTIONS BEFORE COMPLETING FORM

1. REPORT NUMBER
MTL TR 92-24

2. GOVT ACCESSION NO.

3. RECIPIENT'S CATALOG NUMBER

4. TITLE (and Subtitle)
SINGLE CRYSTAL GROWTH OPTIMIZATION OF MAGNESIUM-DOPED LITHIUM NIOBATE

5. TYPE OF REPORT & PERIOD COVERED
Final Report - Sep 88 to Dec 91

6. PERFORMING ORG. REPORT NUMBER

7. AUTHOR(s)
R. G. Schlecht,* C. I. Zanelli,* A. M. Schlecht,* P. F. Bordui,† C. D. Bird,† and R. Blachman†

8. CONTRACT OR GRANT NUMBER(s)
DAAL04-88-C-0029

9. PERFORMING ORGANIZATION NAME AND ADDRESS
*LaserGenics Corporation
2362 Qume Drive, Suite E
San Jose, CA 95131 (SEE BLOCK 18.)

10. PROGRAM ELEMENT, PROJECT, TASK AREA & WORK UNIT NUMBERS

11. CONTROLLING OFFICE NAME AND ADDRESS
U.S. Army Materials Technology Laboratory
Watertown, MA 02172-0001
ATTN: SLCMT-PR

12. REPORT DATE
April 1992

13. NUMBER OF PAGES
45

14. MONITORING AGENCY NAME & ADDRESS (if different from Controlling Office)

15. SECURITY CLASS. (of this report)
Unclassified

15a. DECLASSIFICATION/DOWNGRADING SCHEDULE

16. DISTRIBUTION STATEMENT (of this Report)

Approved for public release; distribution unlimited.

17. DISTRIBUTION STATEMENT (of the abstract entered in Block 20, if different from Report)

18. SUPPLEMENTARY NOTES

†Crystal Technology, Incorporated, 1040 East Meadow Circle, Palo Alto, CA 94303
Presented at 38th Army Sagamore Conference, Plymouth, MA, Sept. 1991.
William A. Spurgeon (COR)

19. KEY WORDS (Continue on reverse side if necessary and identify by block number)

Lithium niobate (doped)
Crystal growth
Optical properties
Nonlinear optics
Photorefractive effect

20. ABSTRACT (Continue on reverse side if necessary and identify by block number)

(SEE REVERSE SIDE)

DD FORM 1 JAN 73 1473 EDITION OF 1 NOV 65 IS OBSOLETE

Block No. 20

ABSTRACT

The purpose of the Phase II program entitled "Single Crystal Growth Optimization of Magnesium-Doped Lithium Niobate" was to optimize the growth of MgO:$LiNbO_3$. The first step in this direction consisted of developing means and methods to accurately measure absorption losses (scattering loss methods were previously developed under a Phase I contract). It was known at the outset that very sensitive instrumentation would be required to allow measurements on small samples. The results of the measurements of both types of photon loss would then be used to optimize the molar concentration of MgO in $LiNbO_3$ to achieve crystals with low loss as well as high photorefractive damage threshold.

Highly sensitive scattering and absorption facilities were developed and used in the process of optimizing crystal growth. The ability to accurately and routinely measure these parameters has allowed us to understand variability in the growth process, determine growth parameters, and --most importantly-- to observe that specific propagation and polarization directions are significantly less lossy than others.

Studies were performed on the growth, poling, and resulting properties of MgO-doped lithium niobate. Both photorefractive damage threshold and NLO phase-matching temperature were observed to vary with MgO concentration. For one crystal doped with a high MgO concentration, it was impossible to induce measurable photorefractive damage.

TABLE OF CONTENTS

LIST OF ILLUSTRATIONS

LIST OF TABLES

1 PROGRAM OVERVIEW

1.1 ABSTRACT

The purpose of the Phase II program entitled "Single Crystal Growth Optimization of Magnesium-Doped Lithium Niobate" was to optimize the growth of $MgO:LiNbO_3$. The first step in this direction consisted of developing means and methods to accurately measure absorption losses (scattering loss methods were previously developed under a Phase I contract). It was known at the outset that very sensitive instrumentation would be required to allow measurements on small samples. The results of the measurements of both types of photon loss would then be used to optimize the molar concentration of MgO in $LiNbO_3$ to achieve crystals with low loss as well as high photorefractive damage threshold.

Highly sensitive scattering and absorption facilities were developed and used in the process of optimizing crystal growth. The ability to accurately and routinely measure these parameters has allowed us to understand variability in the growth process, determine growth parameters, and --most importantly-- to observe that specific propagation and polarization directions are significantly less lossy than others.

Studies were performed on the growth, poling, and resulting properties of MgO-doped lithium niobate. Both photorefractive damage threshold and NLO phase-matching temperature were observed to vary with MgO concentration. For one crystal doped with a high MgO concentration, it was impossible to induce measurable photorefractive damage.

1.2 BACKGROUND

Single crystals of high optical quality have an increasingly important role in electro-optics as these devices become widespread in military and commercial systems. As a consequence, more exacting specifications are being placed on these components in order to achieve optimum results.

Lithium niobate ($LiNbO_3$) is presently used for electro-optic Q-switches, harmonic generators, acousto-optic devices, transducers, modulators, optical parametric oscillators and amplifiers and optically bistable devices. It is one of the key elements in Nd:YAG lasers which are in rangefinders and target designators used by the Army. The optical quality of the material is of critical importance as it determines the reliability and performance of these devices: at present most failures occur within this optical element. One critical parameter is the optical loss caused by the material itself, which can be due to either scattering or absorption. To optimize crystal growth it becomes essential to precisely measure these two losses in order to correlate them to growth conditions. However, before the present program was in place, there was no facility available to reliably and routinely measure the low levels of optical loss in these crystals.

Through the Czochralski process, crystals as large as 150 mm in diameter can be reproducibly grown. High-volume crystal fabrication techniques have been developed enabling high-yield production to demanding tolerances. The use of lithium niobate in optical applications in the near-IR and visible regions of the spectrum has historically been limited due to a phenomenon known as the photorefractive effect (PRE). In PRE, the laser beam itself causes the uncontrolled redistribution of space charges in a crystal. Through the crystal's electro-optic effect, this redistribution gives rise to an uncontrolled refractive index variation that in turn distorts the laser beam. Although such PRE damage generally does not lead to catastrophic crystal failure and can in fact be removed through annealing, its uncontrollability in most cases renders a subject material unsuitable for practical device application.

The doping of $LiNbO_3$ with several mol% of magnesium oxide (MgO) was first reported in 1980 [1] as a means to increase the material's PRE damage threshold. Early work focused on the effect of MgO doping concentrations and identified crystal homogeneity problems associated with a non-unity Mg distribution coefficient.

1.3 OBJECTIVES

There were three major objectives in this Phase II program:

1) Develop and demonstrate the technology to routinely measure the absorption losses in transparent materials with absorption coefficients as low as 10^{-5} m^{-1}.

2) Apply the technology developed in the first objective to measure the optical loss in $MgO:LiNbO_3$ single crystals.

3) To optimize the growth of $MgO:LiNbO_3$ for minimum optical loss and maximized photorefractive damage threshold.

1.4 ACCOMPLISHMENTS

These three tasks have been successfully completed, as is shown in the body of this report. As a result, we have:

- Developed hardware and methods to measure loss in crystals reliably and routinely. The accuracy can be as low as 5×10^{-3} m^{-1} for samples that absorb about 1% at modest power levels. Extension to accuracies of 10^{-5} is possible with higher laser power and larger samples, due to the high resolution of the apparatus (4×10^{-3} °K).

  The equipment and methods are general enough that they can be applied to any transparent material and so could be used to measure the small scattering and absorption losses in a wide variety of materials. This information could then be used to further improve these materials as well, and should lead to an important reduction in the development time.

- Optimized the growth parameters for $MgO:LiNbO_3$ using the Czochralski method, thus making it possible to obtain single crystals that have optimal absorption and PRE characteristics.

- Identified directions of propagation and polarization that cause the least amount of absorption, and at the same time determined that scattering is a minor component of optical loss in $MgO:LiNbO_3$.

2 DEVELOPMENT OF OPTICAL LOSS MEASUREMENT CAPABILITY

Optical losses, as mentioned earlier, can be divided into scattering and absorption. A method was developed during the Phase I of this program to measure scattering loss. During the Phase II this method was further developed for routine testing, although no substantial improvements were required.

2.1 SCATTERING FACILITY

Our scattering loss measurement system is similar to a system recently completed at Stanford University.[2] The system's major components are an integrating sphere, a chopper, and a lock-in amplifier, as shown schematically in figure 1. The laser in the

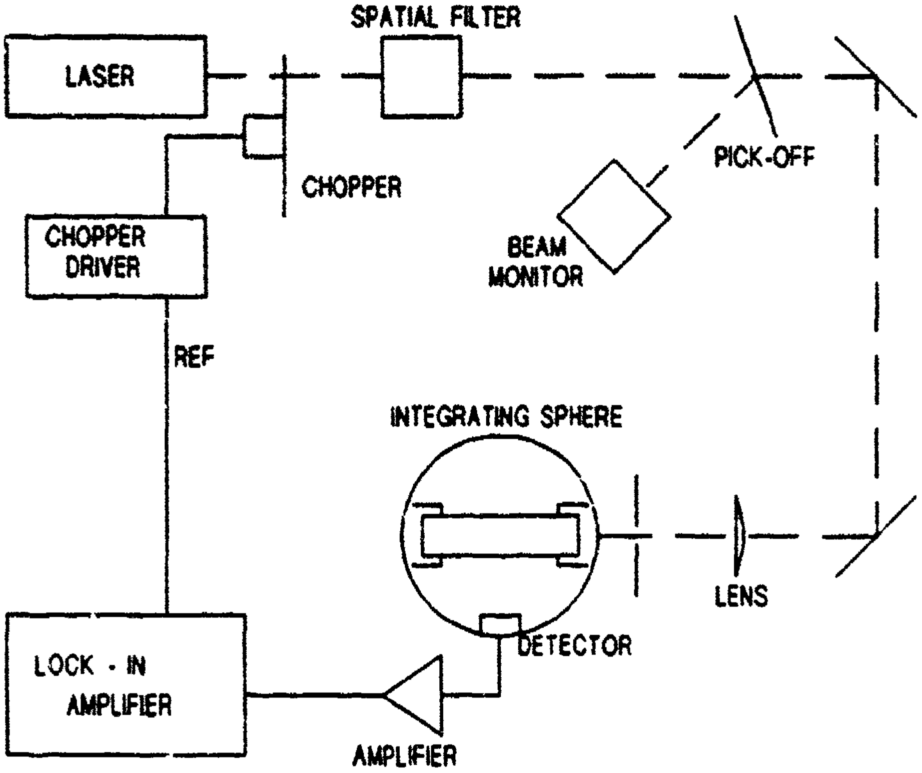

Figure 1. Block diagram of scattering facility.

diagram can be any of several types. We have used He-Ne, argon ion, and Nd:YAG lasers during the course of our investigation. The laser beam is sent through a spatial filter in order to insure a clean Gaussian beam. This is necessary so that the beam will be well defined, can be focused to a well-defined spot and will be as noise-free as possible. The laser beam is then sent through the optical chopper which also sends a reference signal to the lock-in detector. A small fraction of the beam is picked off and sent to a laser beam monitor detector. The beam is then focused into the sample crystal, while apertures are placed in the beam to block out any light that may have been scattered by any of the optical elements in the beam. The laser beam then passes through the sample crystal. The portion of the beam that is scattered by the crystal is captured and reflected by the integrating sphere and is eventually detected by a baffled semiconductor detector. We have used both silicon PIN diodes and InGaAsP detectors. The output from the detector is then amplified and sent to the lock-in amplifier. With this system, depending on the laser used and the laser output power, we have been able to detect a minimum signal of from 125 nanovolts to 1.26 microvolts with laser input powers of from 170 μW to 1.6 mW. A photograph of the apparatus is shown in figure 2 and a photograph of the opened integrating sphere is shown in figure 3.

Figure 2. Photograph of the scattering facility.

2.1.1 Scattering measurements -- methods.

The measurement technique involves placing the material sample within the integrating sphere and focussing the laser radiation through the sample. If both sample end faces are not allowed to reflect light directly into the integrating sphere, only light scattered within the sample bulk is measured by the detector.

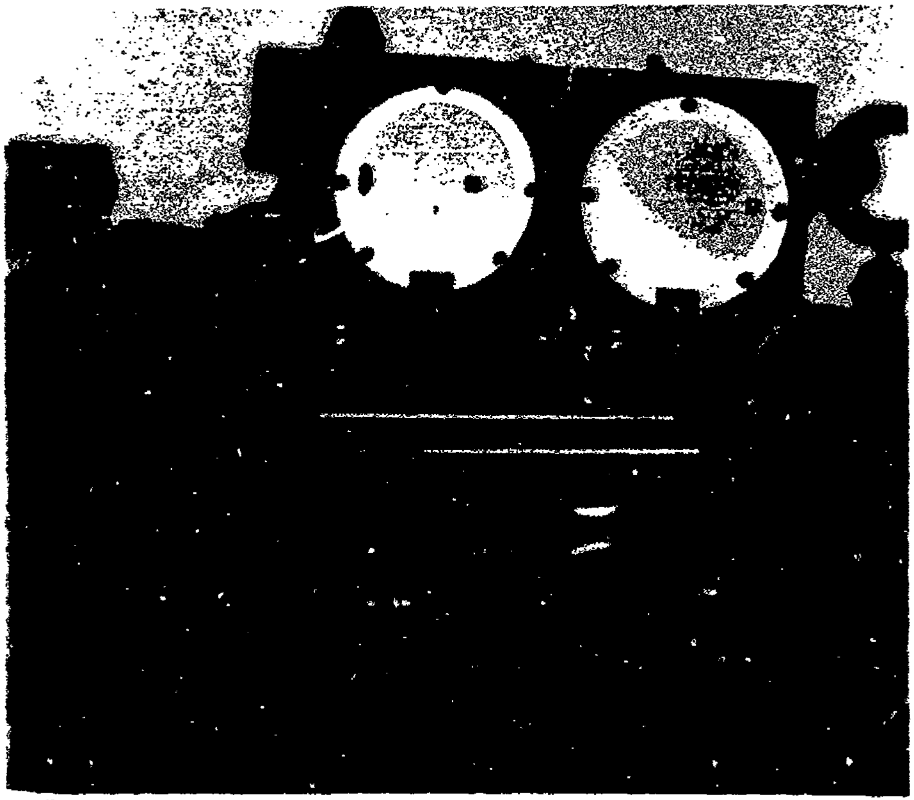

Figure 3. Photograph of the integrating sphere for scattering measurements.

Some early experimentation with index matching oils on the faces to eliminate back reflections into the integrating sphere indicated that the need for "zero" scattering light guides does not warrant using these oils. The difficulties encountered in handling the samples and keeping the integrating sphere free from oil do not compensate the possible gains in measurement accuracy. We chose to try to separate that part of the detected signal due to this backscattered light from the total signal by measuring the scattered signal for a central region of the crystal within the integrating sphere. Internal baffles and highly reflective internal surfaces direct the scattered light toward a detector which is mounted on the integrating sphere. The signal measured on this detector gives the relative magnitude of the scattered light.

Blocking the exit port and measuring the detector's signal gives a relative measure of the total power into the sample. Comparison of the signal obtained with the sample in and out of the sphere gives an absolute determination of the optical scattering losses. Chopping the laser allows phase-sensitive detection which enhances the signal-to-noise ratio at low scattering levels. With the appropriate detector and reflective coatings within the integrating sphere any CW laser can be used in this test apparatus.

We should point out that this apparatus is very flexible and can be used to measure the scattering losses of any transparent material.

2.1.2 Scattering measurements -- data

Because the samples showed a very small scattering coefficient (about 0.005 1/m), we opted to use a He-Ne laser beam rather than a YAG laser due to the higher cross section at shorter wavelengths. The extreme sensitivity of the sensor, on the other hand, made it more convenient to use this low power source instead of a 10 W Argon ion laser. All the measurements reported here were performed with a 5 mW He-Ne laser (632.8 nm) beam focused to approximately 50 μm in diameter.

Figure 4 shows the atomic arrangement of $LiNbO_3$, and the measured scattering coefficients are summarized in table 1. The measurements of the first z-grown crystals available, Z-1 through Z-4, were found later to be in error due to a saturation of the amplifier. At that point a new formulation was announced, whereby a more closely congruent mixture of Li to Nb would be used, and for this reason the measurements were not redone in these samples. Having corrected the saturation problem, we performed the measurements on crystals prepared from boules Z-5 on.

No clear differences could be noticed between Z-, Y- or X-grown crystals, except for the obvious defects that could be observed in the boules (Y-4 and Y-5, for instance). There is a clear difference, however, in the scattering observed for Z-propagation compared to any of the other two directions. Although a slight difference is observed in the absorption coefficients (see below) with different polarizations, this was not observed for scattering. Contrary to expectations, striae were not found to have a major effect on scattering, suggesting that the index modulation is very small compared to other causes. Figure 5 contains the data from table 1, having grouped all polarization and growth axis together, and differentiating only on the basis of propagation directions: either Z- or non-Z axis propagation.

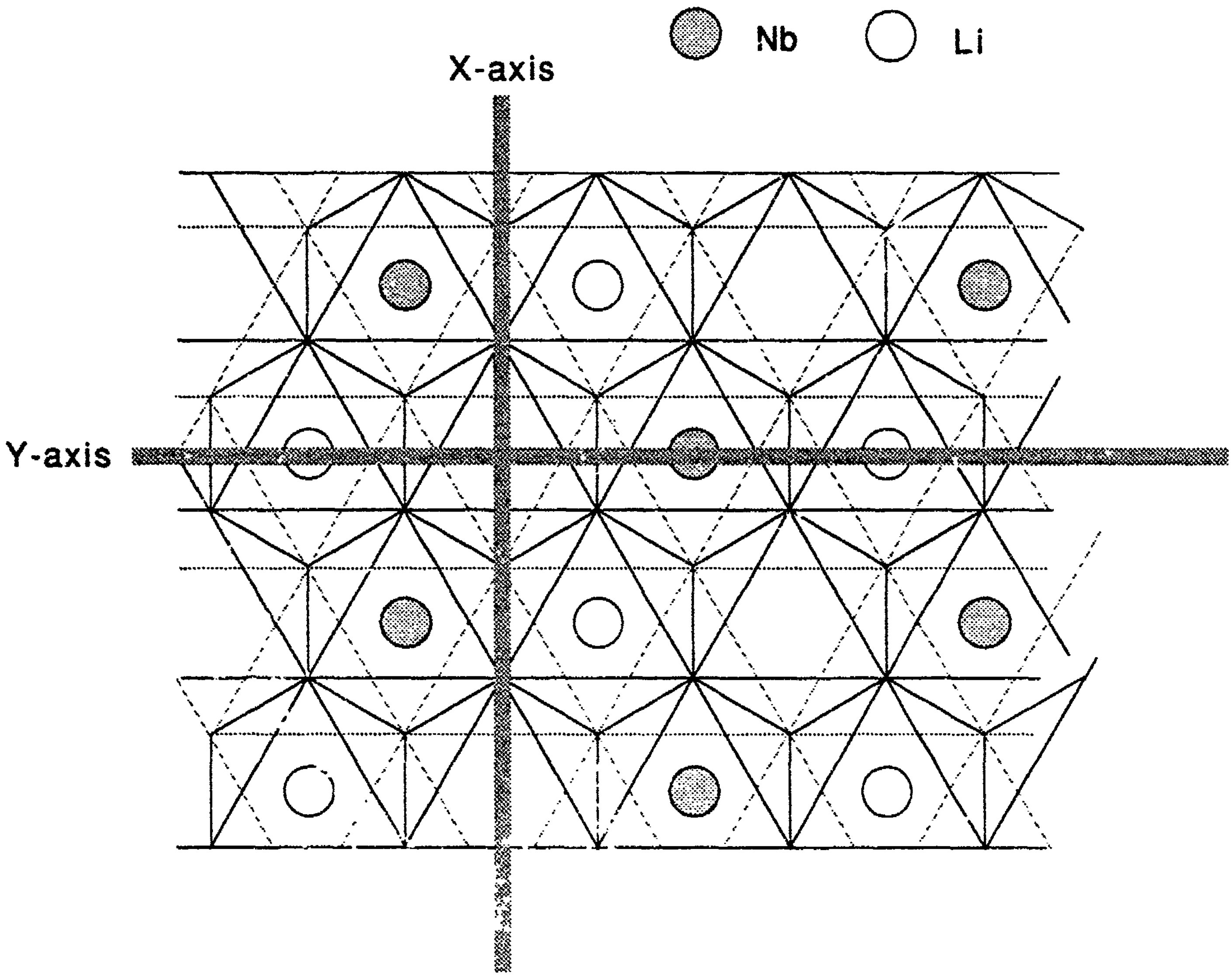

Schematic atomic arrangement in the basal (0001) plane of lithium niobate. The oxygen sublattice is represented by lines connecting nearest-neighbor oxygen centers; the two layers of oxygen atoms sandwich the cations into octahedral sites. Note that there exist three symmetrically equivalent sets of Cartesian x- and y-axes; only one is shown.

Figure 4. Cartesian axis definition for $LiNbO_3$

Table 1. Summary of scattering coefficients [1/m] at 632.8 nm.

PROPAGATION >			Z	==== X OR Y ====		
POLARIZATION >			X OR Y	Y OR X	Z	ANY
BOULE	[Li$_2$O]	[MgO]	AVG	AVG	AVG	AVG
Z-5	48.60	4.65	0.027	0.006	0.008	0.007
Z-6	48.38	4.70	0.032	0.017	0.021	0.019
Z-7	48.38	4.80	0.017	0.005	0.006	0.005
Z-8	48.38	4.90	0.025	0.006	0.005	0.005
X-3	48.38	3.00	0.019	0.006	0.008	0.007
Y-1	48.38	4.70	0.019	0.006	0.009	0.008
Y-2	48.38	4.80	0.011	0.009	0.009	0.009
Y-3	48.38	3.00	0.017	0.008	0.008	0.008
Y-4	48.38	4.90	0.105	0.061	0.049	0.055
Y-5	48.38	5.10	0.149	0.139	0.124	0.132

Avg indicates average over all samples in each boule.

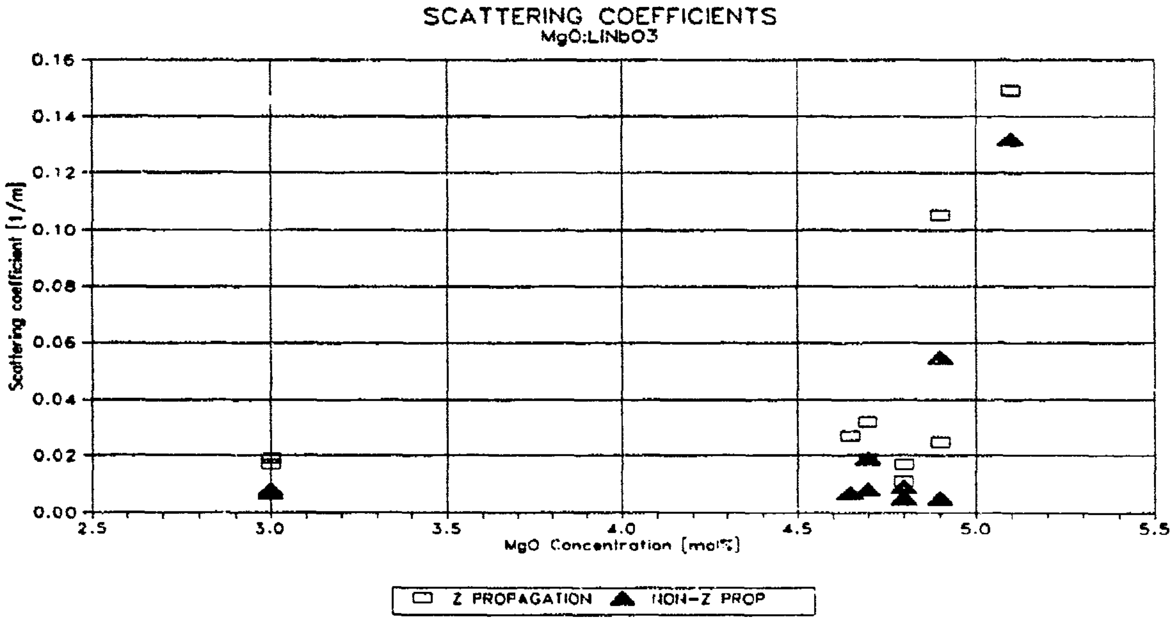

Figure 5. Scattering coefficient for all crystals, all polarizations.

2.2 CALORIMETRIC PHOTO-ABSORPTION FACILITY

2.2.1 Calorimetry of photo-absorption

The flow of energy into and out of a crystal cell is schematically shown in figure 6. The

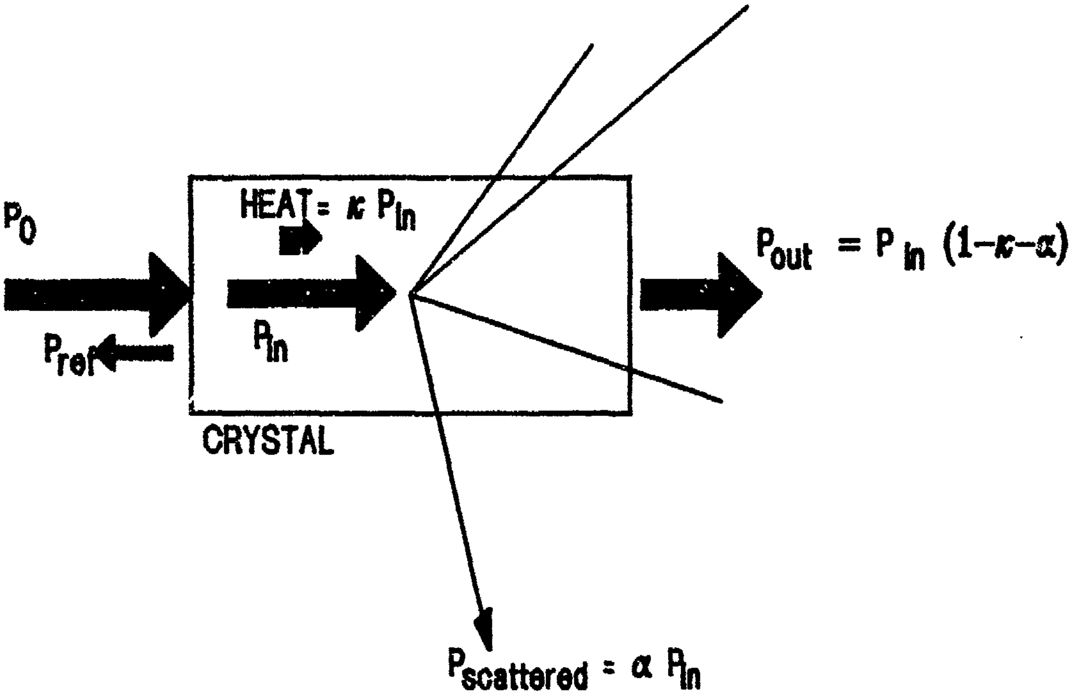

Figure 6. Energy flow diagram for photoabsorption in a crystal.

index of refraction n determines the amount of energy that enters the crystal, P_{in}, and the fraction converted into heat (inelastic scattering) is κ P_{in}. Another fraction is elastically scattered, leaving the cell. As a consequence of these two losses, the beam intensity decreases exponentially along its path:

$$I(x) = I_0 e^{-(\lambda + \sigma)x}$$

where the constants λ and σ correspond to absorption and scattering, respectively. The energy deposited in the crystal by absorption raises its temperature as a function of time. The absorption coefficient λ, is given by the path length L and the converted fraction κ as

$$\lambda = (1/L) \ln [(T - R\kappa) / (T - \kappa)]$$

where T and R are the transmission and reflection coefficients for the crystal face. The appendices contain details of this derivation and the means to convert the time dependence of temperature into κ.

Measuring the absorption coefficient was accomplished with a very sensitive calorimetric photo absorption apparatus, described schematically in figure 7.

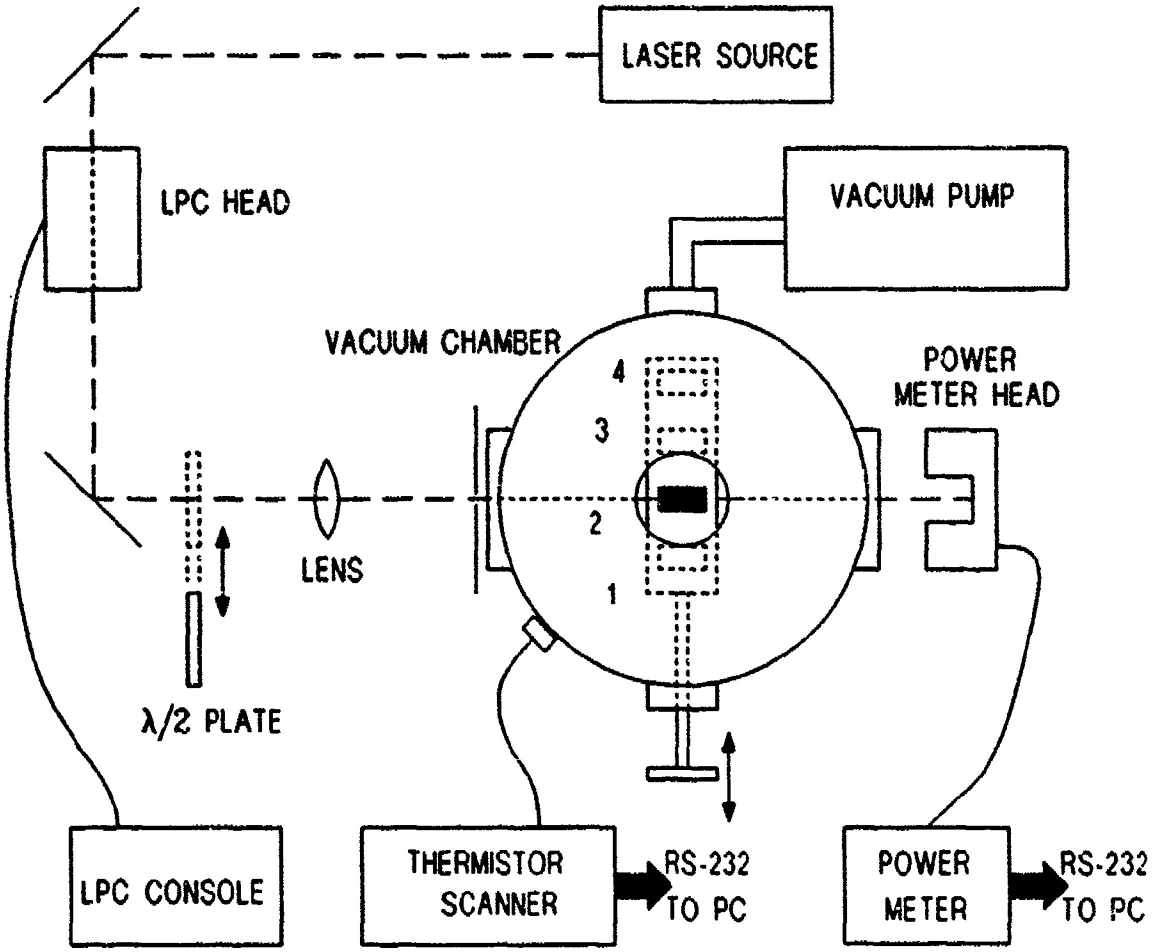

Figure 7. Schematics of the calorimetric absorption spectroscopy setup.

A vacuum chamber, in conjunction with a turbomolecular vacuum pump, create an environment free of convection and air conduction losses for the samples, by sustaining them at pressures below 10^{-4} Torr. Light generated by a laser is stabilized by a Laser Power Controller (LPC), to insure that the delivered power is constant throughout the active absorption period. The beam is then collimated and focused into the samples (numbered 1 to 4) and its intensity is monitored by the laser power meter.

The vacuum chamber is made of stainless steel with entrance and exit windows, a top-view window to facilitate sample location, a mechanical feedthrough to move the samples in and out of the beam, and electrical feedthroughs for temperature monitoring.

The sample holder (see figure 8) consists of a frame on which four samples can be supported by a grid of 60 μm nylon fibers. The limited contact surface not only reduces the loss, but also reduces variations among samples of different mass.

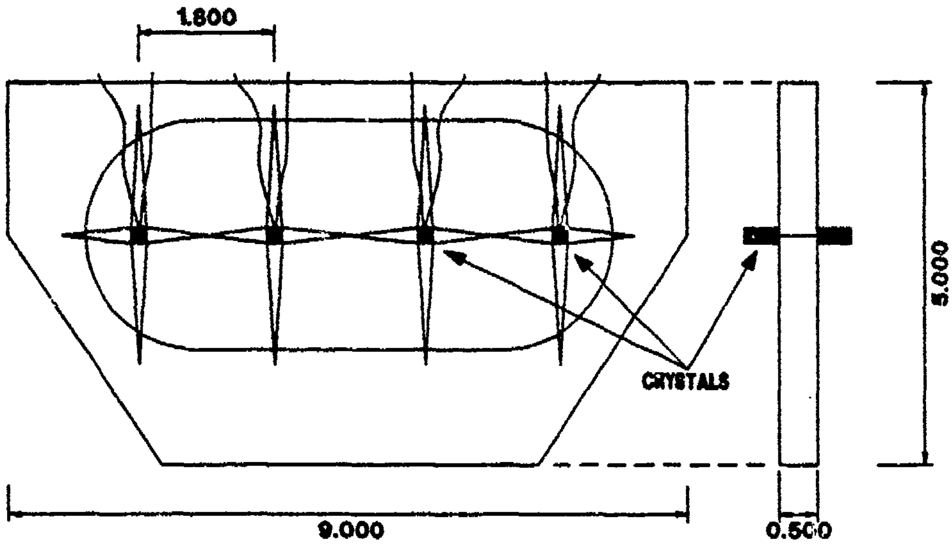

Figure 8. Frame used to hold samples in absorption measurements. Dimensions in inches.

To prevent the beam from touching the other walls of the cell or the thermistor itself, it is important to ensure that the beam diameter is safely contained within the sample, including at least two of the Fresnel reflections. This was achieved by having a beam diameter of less than 500 μm, while the crystal dimensions were at least 6 × 7 mm. The inclusion of the Fresnel reflections was insured during sample alignment using a He-Ne pilot beam.

The temperature of each crystal sample is monitored by low-mass thermistors, typically 60 mg, attached to the middle of one of the sides with Tra-Con 2902 Ag epoxy (for good

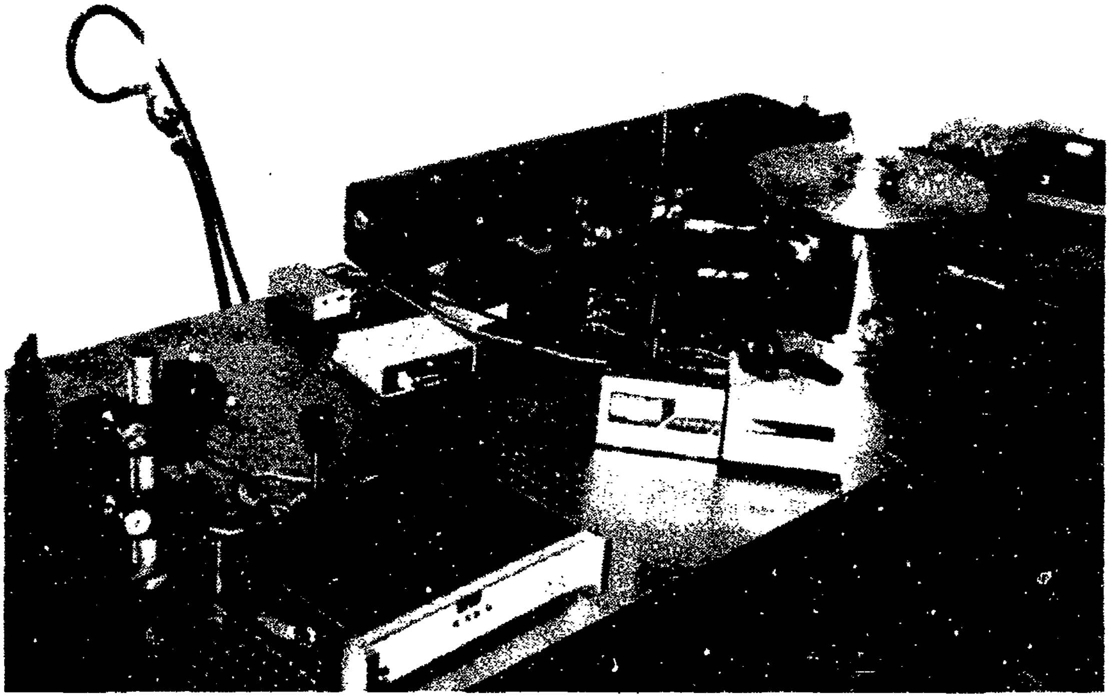

Figure 9. Photograph of calorimetric absorption facility.

thermal conductivity). As the mass of the crystals used was between 4 and 8 grams, a small correction (always below 0.6%) was made for the thermistor/epoxy mass contribution (see Appendix A for details). The thermistors chosen, YSI 44037 and Alpha Thermistor Inc., part # 13A6001-D3, have a nominal resistance of 6 KΩ at 25 °C (to minimize lead resistance effects), and high $\delta R/\delta T$ sensitivity. Long, thin leads (.004" diam.) attach the thermistors to the apparatus to minimize loss through this thermal connection.

The resistance is measured (accurate within the equivalent of 4×10^{-3} °C) with a scanning ohmmeter (Azonix ScannerPlus equipped with thermistor cards) that measures voltage generated by a $10\mu A$ DC current. It then converts the measured value to ASCII code for transmission via RS-232 to a PC. The Azonix scanning ohmmeter is capable of sampling up to four channels every two seconds.

Two light sources were employed. Initially, an Argon-ion laser tuned to 476, 488 and 514.5 nm was used and later a YAG laser was employed for the bulk of measurement as absorption at 1064 nm is more relevant to $LiNbO_3$ applications. The beam was normally polarized (95%) along a horizontal plane, and sensitivity to polarization was studied by rotating the polarization with a $\lambda/2$ plate.

Laser power (in the range of 200 - 500 mW) was monitored with an Ophir Optics DG

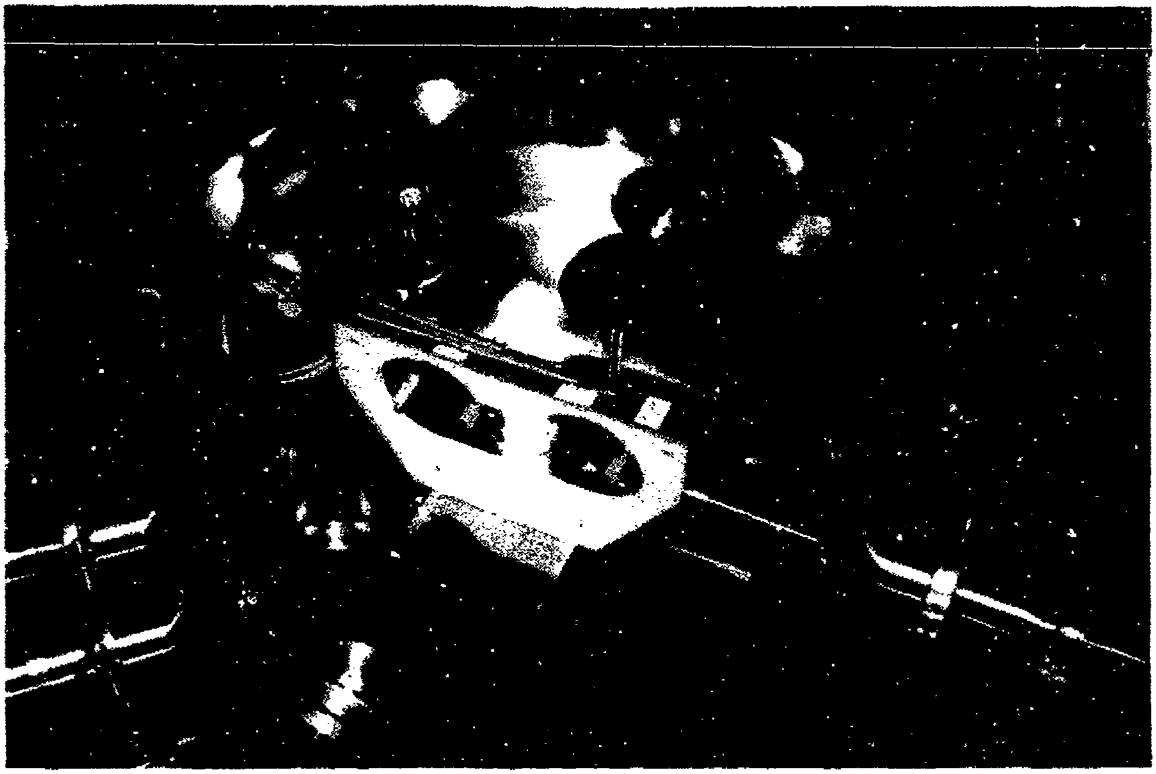

Figure 10. Photograph of the absorption facility vacuum chamber.

laser power meter. Its stated accuracy at the operating range used is 5 mW, equipped with A-D-Serial circuitry for logging the data on the PC.

2.2.2 Measurements

Six parameters are monitored by the computer: time (seconds), laser power (mW), and resistances of all four thermistors (Ohms). The data acquisition program performs measurements about every 500 ms, and records a measurement (writes it into a data file) if any of the above parameters differs from the prior recorded value by more than a presettable threshold. This allows faster sampling when the temperatures change rapidly, or when power variations are detected (turning laser on or off), or at maximum time intervals, while keeping the amount of data to a manageable size.

The program computes temperatures from the resistance values using the Steinhart and Hart equation[3] and coefficients obtained from the calibration curves provided by the manufacturers (YSI and Alpha Thermistor Inc.). These four temperature values are appended to the six raw data points for each observation.

The data analysis uses the statistical methods outlined in appendix A, based on the following experimental conditions:

- Laser power is kept constant during the heating period to within 1%
- Vacuum is kept below 10^{-4} Torr throughout heating and cooling
- Heating is applied for a time at least as long as the cooling time constant.

Preliminary runs were made using two thermistors attached to a single crystal, one in the center and one near the entrance point, as shown in figure 11.

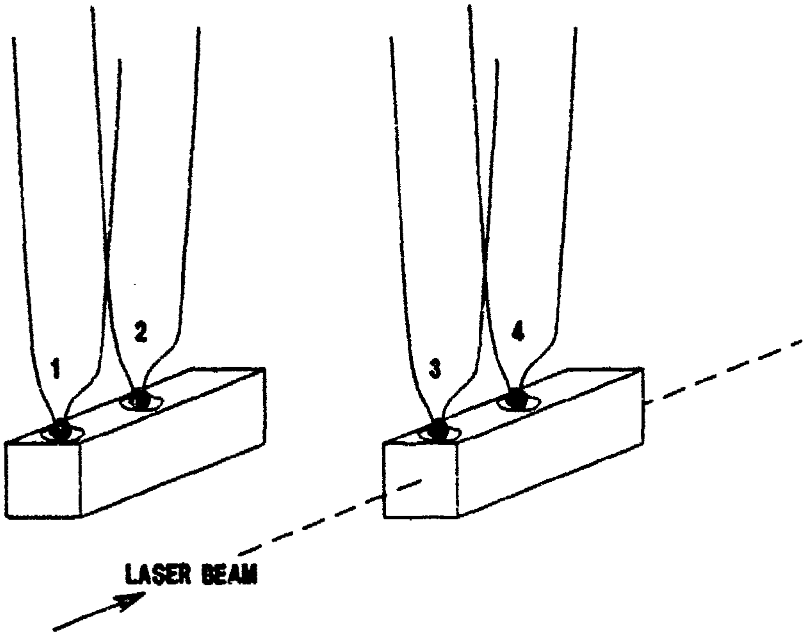

Figure 11. Two-thermistor configuration used during system checkout.

The resulting thermal measurement illustrates the level of sensitivity of the instrumentation. We measured four temperature values (two per crystal) on two crystals of the same dimensions. The first crystal, monitored by thermistors 1 and 2, was not exposed to the beam. The second crystal (monitored by thermistors 3 and 4) was exposed to a 1.3 W (CW) beam at 1064 nm. As shown in figure 12, the beam was on from t = 20 to t = 1400 seconds, and was quite stable.

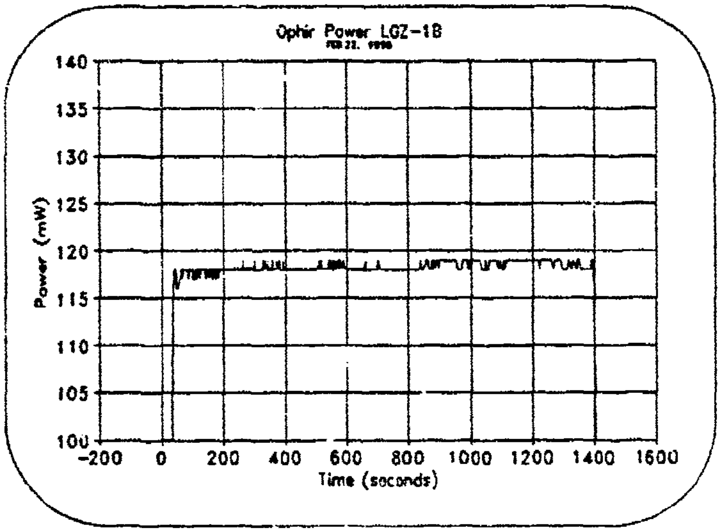

Figure 12. Typical mea:urement of laser power.

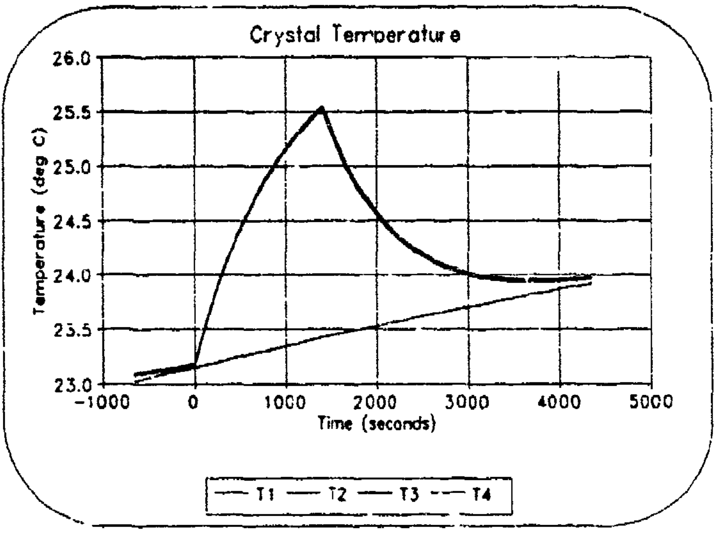

Figure 13. Raw temperatures for all four thermistors depicted in figure 11.

The raw temperatures shown in figure 13 indicate a slight drift throughout the chamber, as indicated by the reference thermistors 1 and 2.

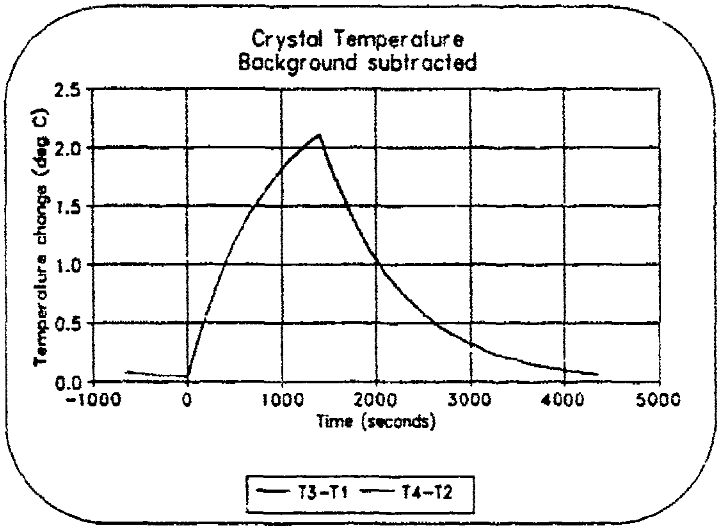

Figure 14. Temperatures near the front surface (T3-T1) and at the center of the crystal (T4-T2).

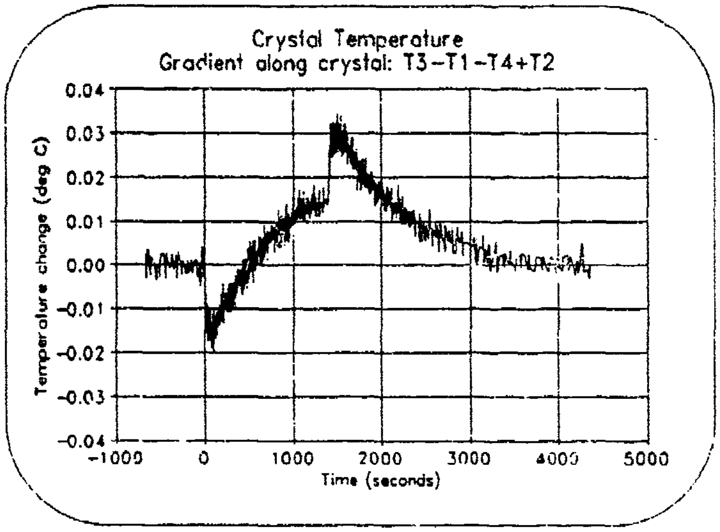

Figure 15. Temperature gradient: front face to middle of crystal sample.

When the reference temperatures are subtracted, the temperature changes due to the beam can be observed, as shown in figure 14. Both curves (T3-T1) and (T4-T2) match quite closely except for a small offset due to variations intrinsic to the sensors. This offset can be observed under no power, averaged over some time, and subtracted from each thermistor's readings.

The difference (T3-T4)-(T1-T2) is plotted in an enlarged scale in figure 15, where a slight temperature gradient along the crystal can be observed. The curve shows that the end of the rod (T3) warms up more rapidly than the bulk (T4) at the beginning, probably due to surface imperfections, until equilibrium is reached and thereafter the end stays cooler than the bulk (more access to radiative surface). The effect is reversed when the laser is turned off.

Figure 16 shows a typical computer printout for a single measurement of absorption coefficient. The values used for all the calculations are present in each printout, as well as graphical information on the exponential fits.

2.2.3 Uncertainties

Several uncertainties have a role in the measurement of the absorption coefficient λ, and not all contribute in a predictable way to the final accuracy of the measurements. Direct measurement errors come from the following sources:

P_0 - Incident power. Known to 1% relative, 3% absolute.
C_E - Crystal heat capacity. Not known for MgO doped $LiNbO_3$, and assumed the same for all crystals to be 0.654 [J/g-°C], the value for undoped $LiNbO_3$.
L - Light path length. Typically 25 mm, known $\pm$ 5 μm.
n - Crystal index of refraction. Assumed for all crystals to be 2.25.
m - Crystal mass. Typically 4 - 6 g, known within $\pm$ 2mg.

Other aspects contribute to the total uncertainty, such as cleanliness of the crystal and window surfaces, beam purity and alignment, and drift in the measuring equipment. As expected, these less quantifiable components of the total uncertainty contribute the most. As a test of reproducibility, the same sample was reinstalled and measured throughout the 14 months of measurements, yielding a value that oscillated between 0.194 and 0.199 [1/m]. We believe that this represents the experimental (random) uncertainty in the results, estimated for all samples at about 0.005 [1/m]. Systematic errors (for example, if the assumed values for C_E and n were found in error) affect all measurements -- and can be corrected for, should new values appear more accurate. For the purpose of optimizing crystal growth, however, systematic errors do not alter the conclusions as the dependency of λ is monotonic.

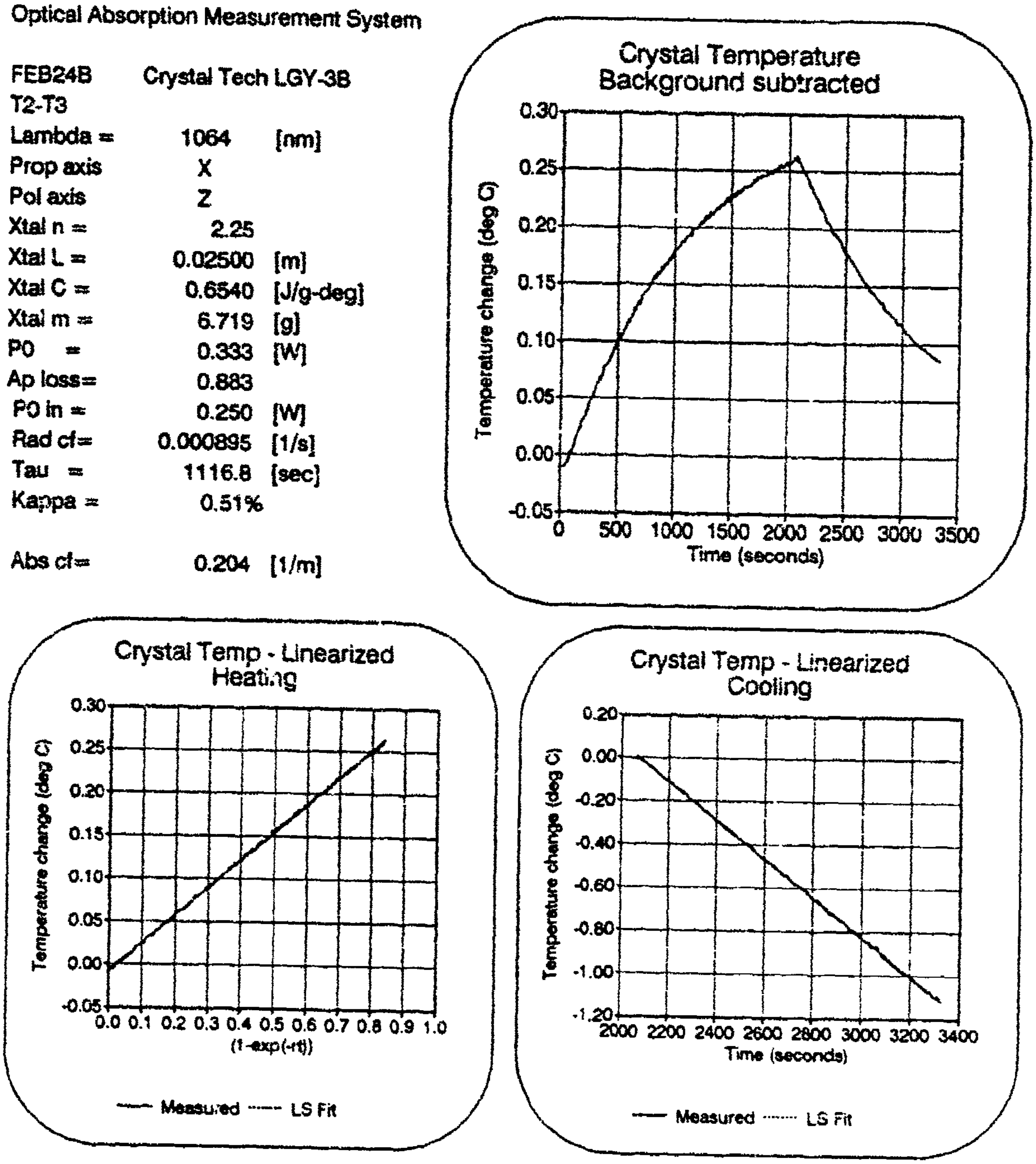

Optical Absorption Measurement System

FEB24B Crystal Tech LGY-3B
T2-T3

Lambda =	1064	[nm]
Prop axis	X	
Pol axis	Z	
Xtal n =	2.25	
Xtal L =	0.02500	[m]
Xtal C =	0.6540	[J/g-deg]
Xtal m =	6.719	[g]
P0 =	0.333	[W]
Ap loss=	0.883	
P0 in =	0.250	[W]
Rad cf=	0.000895	[1/s]
Tau =	1116.8	[sec]
Kappa =	0.51%	
Abs cf=	0.204	[1/m]

Figure 16. Typical computer printout for absorption measurements.

2.3 RESULTS

Table 2 shows the samples obtained for each grown boule, their corresponding compositions, and the measured values of absorption coefficient along the various axis, differentiating among 1) propagation along the Z axis, any polarization, 2) propagation perpendicular to the Z axis, polarization parallel to Z axis, and 3) propagation perpendicular to the Z axis, polarization perpendicular to Z axis.

Table 2. Summary of absorption coefficients [1/m] at 1064 nm.

PROPAGATION >			==== Z ====		====== X OR Y ======			
POLARIZATION >			X OR Y		Y OR X		Z	
BOULE	[Li_2O]	[MgO]	AVG	U	AVG	U	AVG	U
Z-1	48.60	4.80	0.231	6.6	0.075	7.5	0.037	2.6
Z-2	48.60	4.70			0.109		0.052	
Z-3	48.60	4.60	0.155		0.110	5.2	0.050	8.3
Z-4	48.60	4.50	0.179		0.089		0.046	3.8
Z-5	48.60	4.65	0.133	7.4	0.057		0.044	
Z-6	48.38	4.70	0.175	2.5	0.112		0.053	
Z-7	48.38	4.80	0.150		0.116			
Z-8	48.38	4.90	0.127		0.101			
X-3	48.38	3.00	0.158		0.132			
Y-1	48.38	4.70	0.164		0.131			
Y-2	48.38	4.80	0.266	3.6	0.246		0.114	
Y-3	48.38	3.00			0.351	8.6	0.222	1.6
Y-4	48.38	4.90	0.124		0.152			
Y-5	48.38	5.10	0.547		0.408			

Avg indicates average over all samples in each boule.
U = Uniformity rating: average value divided by observed range, n≥3.

The same information is shown in figures 17 through 21. The two Li_2O concentrations of 48.60% and 48.38% in the case of Z-grown crystals are plotted in figures 17 to 18.

The more closely congruent composition of 48.38% Li_2O was used for the Y-grown

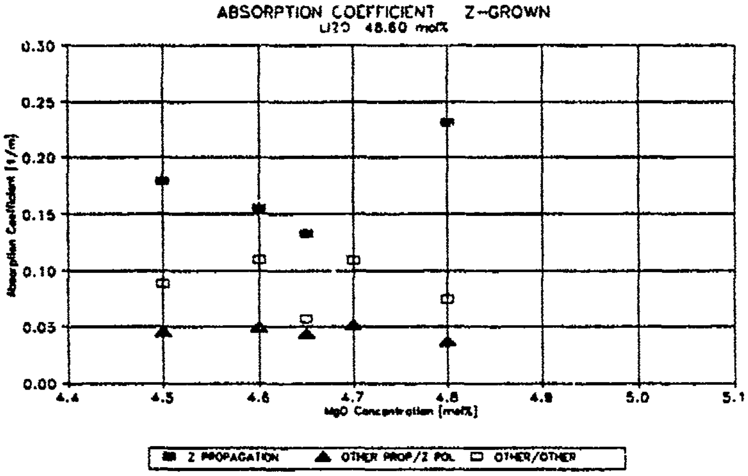

Figure 17. Absorption coefficient for Z-grown boules using the quasi-congruent mixture with 48.60 mol% Li_2O.

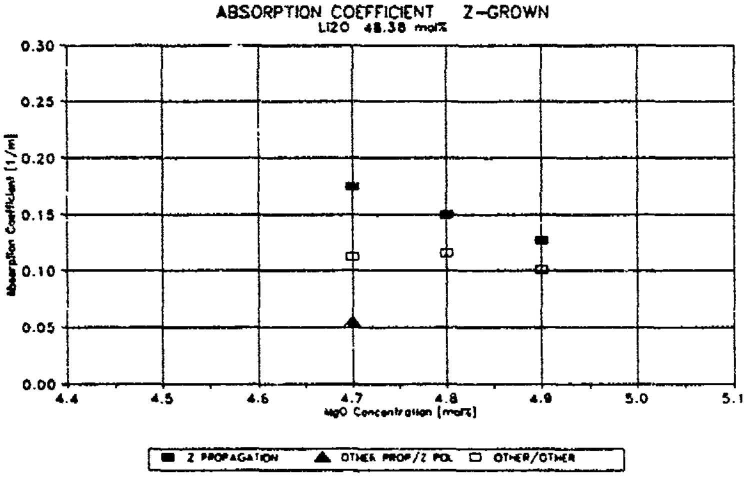

Figure 18. Absorption coefficient for Z-grown boules using the newly developed mixture with 48.38 mol% Li_2O.

c 'stals, shown in figures 19 and 20. In these graphs the measurement error bars are ap roximately the size of the symbols.

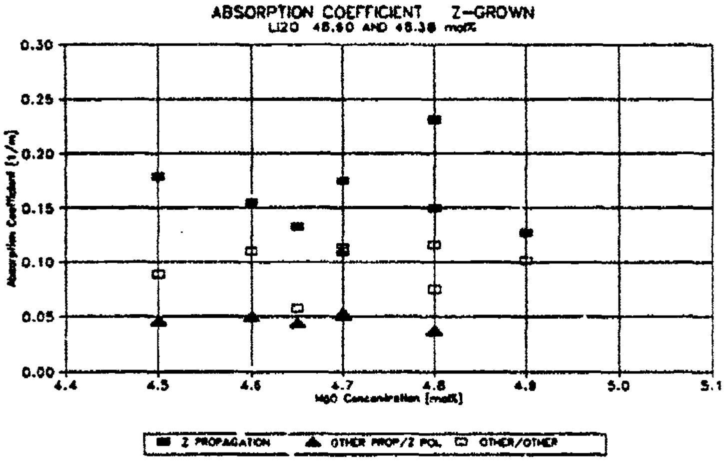

Figure 19. Absorption coefficient for Z-grown crystal. Data for 48.60 and 48.38 mol% combined.

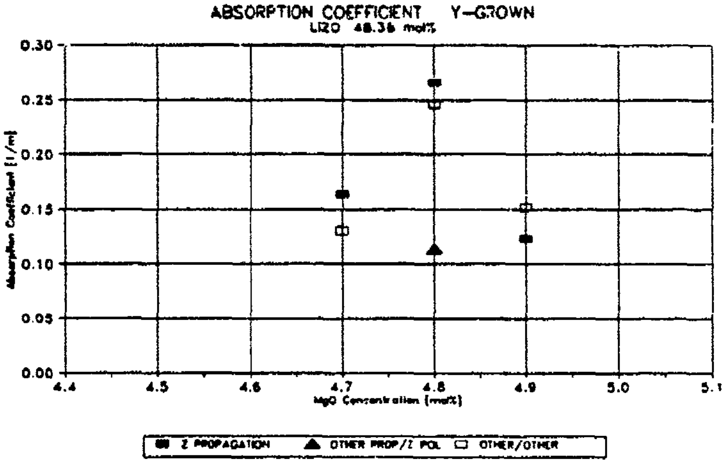

Figure 20. Absorption coefficient for Y-grown boules with 48.38 mol% Li_2O. Subset plotted in the same scale as figure 19 for comparison.

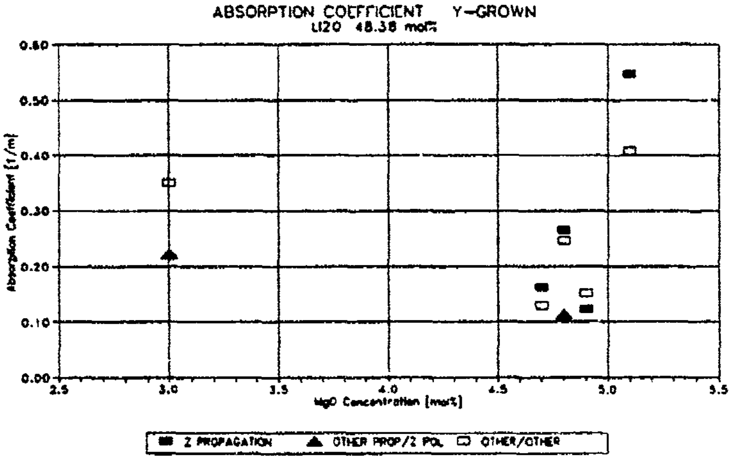

Figure 21. Absorption coefficient for Y-grown $LiNbO_3$.

Comparing figures 17 and 18 does not indicate that the different Li_2O percentage makes a noticeable difference. Based on this observation, data from both formulations were combined into figure 19, where an interesting trend can be seen. It appears that Z-propagation causes the most absorption, whereas Z-polarization causes the least absorption. This is surprising, since the striae are perpendicular to the Z-axis and it was believed that they were a major cause for the increased absorption in $MgO:LiNbO_3$. It is also interesting that within the range of MgO concentrations between 4.5 and 5 mol% there is no visible increase or decrease in absorbance.

A subset of the Y-grown crystal data was plotted in figure 20, at the same scale as figure 19, for comparison purposes. Although the data are scanty, no dramatic difference appears to exist between Z- and Y-grown crystals, except perhaps in the fact that Y-grown seemed more difficult to obtain without cracks or other defects (see Table 1 and figure 5 for scattering results).

Figure 21 contains all the data obtained from Y-grown crystals, in which some extreme MgO concentrations (from 3% to 5.1%) were attempted. The 5.1% data (Y-5) show increased absorption, although it is not clear whether this is due to the increased scattering that this boule exhibits.

3 CRYSTAL GROWTH DEVELOPMENT

The doping of $LiNbO_3$ with several mol% of magnesium oxide (MgO) was first reported in 1980 [1] as a means to increase the material's PRE damage threshold. Early work focused on the effect of MgO doping concentrations and identified crystal homogeneity problems associated with a non-unity Mg distribution coefficient. All of the MgO-doped lithium niobate crystals reported to date with MgO concentrations in the vicinity of 5 mol% have been found to contain planar striae, perpendicular to the growth direction with thickness and spacing on a sub-millimeter scale. These striae appear to be due to microscopic fluctuations in the MgO concentration, corresponding to periodic microscopic instabilities in the crystal growth and dopant incorporation processes. Without engaging in a broad-based research effort to investigate the details of the time-dependent dopant incorporation phenomena occurring at the growth interface, it seems unlikely that the formation of such striae could be eliminated or even significantly limited.

For certain applications of interest, optical interactions in directions parallel to the striae can result in undesirable beam scattering effects. Of particular interest is noncritical phasematching to achieve frequency doubling of a 1.06 μm Nd:YAG laser beam. It has been shown that such an application would preferably be addressed through use of a doubling crystal with its striae oriented parallel to the Z-direction. Such a crystal would, therefore, require its growth axis to lie in the X-Y plane.

Due to the non-unity distribution coefficient of the Mg dopant, MgO-doped $LiNbO_3$ crystals exhibit both short-range and long-range composition variations. The short-range variations took the form of periodic planar striae oriented perpendicular to a crystal's growth direction with a spacing of roughly 200 μm. These striae result in severe scatter losses for laser propagation in directions perpendicular to a crystal's growth axis. On the other hand, a long-range composition variation was observed to result in a slow change in a crystal's birefringence along the direction of its growth axis. This in turn was observed to limit the effective usable crystal length for laser propagation in the direction parallel to the crystal's growth axis. It thus appeared that the incongruency of the growth process for $MgO:LiNbO_3$ might entail inherent limitations for application-related material quality.

The aim of the present work was to study the growth, poling, and resulting properties of $MgO:LiNbO_3$. Ferroelectric poling conditions were studied and refined. Growth-induced striae were observed for all crystal orientations. Achievable freedom from grown-in strain was found to depend strongly on growth orientation. Over the range of conditions studied, optical losses were found to not depend strongly on MgO concentration or growth orientation. Photorefractive damage threshold was observed to be a function of temperature and laser fluence. Growth parameters investigated included MgO concentration in the melt, growth orientation, and basic Czochralski growth conditions. Ferroelectric poling conditions were studied and refined. Crystals were analyzed for

MgO concentration, strain state, IR transmission, scattering and absorption loss, PRE damage threshold, and nonlinear optical (NLO) phase-matching properties. The discontinuous shift in the IR absorption peak associated with residual OH^- appeared to be an important indicator of dramatic optical property changes in the material.

3.1 CRYSTAL GROWTH RUNS

Sixteen growth runs were performed, all by the Czochralski technique. The resulting boules averaged roughly 80 mm in diameter by 50 mm in length. Basic charge preparation and crystal growth procedures were essentially the same as those used in the production of optical-grade undoped $LiNbO_3$. MgO powders were screened through spark source mass spectrometry to ensure chemical purity, after a drying procedure was refined for this material.

Table 3 summarizes the crystal growth experiments. The third letter in the "Boule #" designation indicates the growth axis. Crystals were grown along the x, y, and z axes. Two different Li/Nb ratios were used in the course of the experiments. The 48.60 mol% Li_2O composition had been the industry standard for "congruent" undoped $LiNbO_3$ at the time of this project's initiation. While this project was underway, parallel work at CTI identified a corrected value of 48.38 mol% for the actual congruent composition for undoped $LiNbO_3$ [4]. This modified value was then adopted for subsequent MgO:$LiNbO_3$ work. A variety of MgO concentrations were used in doping the crystal growth melts, from 3.0 to 5.1 mol%. Several crystals were analyzed for MgO concentration using DC plasma spectroscopy.

IR transmission scans were performed on each boule as a function of axial position, using a Perkin-Elmer Lambda-9 Spectrophotometer. The technique involved using masking tape to define 3mm square windows immediately below the shoulder of a boule and immediately above the foot.

Ferroelectric Curie temperature measurements were performed on samples from the top and bottom of each boule. The measurement apparatus, based on dielectric effects, has been described previously [5] and is routinely used at CTI to investigate compositional and poling issues in ferroelectric crystals.

Czochralski growth conditions proprietary to CTI were initially based on those used in production of optical-grade undoped $LiNbO_3$ and were then adjusted in an iterative manner. Immediately following growth, each boule was inspected for macroscopic crystal quality using standard production procedures for undoped $LiNbO_3$. In Table 3, "Strain' is rated on a qualitative scale of A, B, C, D. F with "A" representing typical undoped $LiNbO_3$ suitable for Q-switch application per CTI specifications, "B" represents quality slightly below standard, etc. to "F" representing material not likely to survive a poling operation. "Scatter" is an estimate of the number of particles in a 25 mm length of

Table 3. Summary of growth runs.

Boule #	[Li_2O] mol%	[MgO] mol%	IR Scan Top	IR Scan Bottom	Tc (°C) Top	Tc (°C) Bottom	Strain	Scatter	Comments
LGZ-1	48.60%	4.80%	2.83μm	2.83μm	1221.9° ±0.3°	1221.5° ±0.3°	D	<5/inch	Only a bulk IR scan performed. No distinction between top and bottom of boule.
LGZ-2	48.60%	4.70%	2.83μm	2.83μm	1221.2° ±0.4°	1221.4° ±0.3°	B	None	Only a bulk IR scan performed. No distinction between top and bottom of boule.
LGZ-3	48.60%	4.60%	Both	2.83μm	1220.6° ±0.3°	1221.4° ±0.2°	B	<5/inch	
LGZ-4	48.50%	4.50%	2.87μm	2.87μm	1220.6° ±0.4°	1220.9° ±0.4°	B	<500/ inch	
LGZ-5	48.60%	4.65%	Both	2.83μm	1221.5° ±0.6°	1221.2° ±0.6°	C	<5/inch	
LGZ-6	48.38%	4.70%	2.87μm	2.87μm	1220.6° ±0.2°	1222.1° ±0.3°	B	None	
LGZ-7	48.38%	4.80%	Both	2.83μm	1221.3° ±0.3°	1222.1° ±0.3°	B+	<1000/ inch	
LGZ-8	48.38%	4.90%	2.83μm	2.83μm	1220.8° ±0.3°	1221 ±0.3°	B	None	
LGX-1	48.38%	4.70%	2.87μm	Both	1220.8° ±0.3°	1221.4° ±0.3°	F	None	Heavily cracked boule.
LGX-2	48.38%	4.80%	2.87μm	Both	1221.4° ±0.2°	1221.1° ±0.4°	F	>1000/ inch	Heavily cracked boule.
LGX-3	48.38%	3.00%	2.87μm	2.87μm	1205.1° ±0.3°	1206.0° ±0.3°	D	>1000/ inch	Two planar cracks near the shoulder.
LGY-1	48.38%	4.70%	2.87μm	2.87μm	1219.7° ±0.3°	1220.0° ±0.3°	D	<1000/ inch	Three small cracks in the cone and one in the bulk of the boule.
LGY-2	48.38%	4.80%	2.87μm	2.87μm	1220.0° ±0.3°	1220.9° ±0.3°	D	None	Two planar cracks and one fractured region at shoulder. Bubble inclusions in cone.
LGY-3	48.38%	3.00%	2.87μm	2.87μm	1206.6° ±0.3°	1206.6° ±0.3°	C	None	
LGY-4	48.38%	4.90%	Both	2.83μm	1220.8° ±0.3°	1220.8° ±0.3°	D	~5 total in boule	One planar crack center bottom of boule. Bubble inclusions in cone. This boule smaller than previous ones
LGY-5	48.38%	5.10%	2.83μm	2.83μm	1220.4° ±0.4°	1220.5° ±0.4°	F	>1000/inch	Multiple fracture down one side of boule due to polycrystallinity. ~35% of boule cracked.

crystal detectable with the unaided eye using a white microscope light in a darkened room.

Macroscopic crystal quality was found to be a strong function of the growth axis. Z-axis material was the easiest to grow with low strain. The best boules (B and B+ on our strict grading scale) were only slightly inferior to undoped $LiNbO_3$ used in Q-switch applications. With y-axis and especially x-axis growth, it was discovered that higher effective thermal gradients were necessary to avoid the formation of polycrystallinity. As a consequence, the resulting boules tended to be heavily strained. All three x-axis boules were cracked, two of them severely enough to preclude poling.

In general, for a given axis of growth, a higher MgO melt concentration resulted in lower macroscopic crystal quality. No effect was observed of the relatively small variation in Li/Nb melt ratio.

All of the grown crystals exhibited planar striae perpendicular to the growth axis similar to, although less severe than, those described in the Nightingale work [6]. It is notable that the striae were only visible in light with a polarization component along the crystallographic z-axis. For light polarized in the crystallographic x-y plane, the striae were invisible. Heat treatment up to 50 hours in duration at temperatures in excess of 1200°C appeared to have no influence on reducing the striae. The appearance of the striae did not vary strongly with MgO concentration over the range studied.

Chemical analysis (subcontracted to Ledoux & Co. of Teaneck, NJ) of several boules indicated an effective distribution coefficient for Mg of roughly 1.05. Thus, MgO concentration decreased down the growth axis of each boule.

IR transmission analysis produced surprising results. As expected from Bryan's report[7], boules with the lowest MgO concentration exhibited unshifted (2.87m) OH^- absorption peaks while boules with the highest MgO concentration exhibited shifted (2.83m) peaks. For boules with intermediate MgO concentration, however, boule bottoms tended to have shifted OH^- absorption peaks while boule tops tended to have unshifted peaks. Given the results of the chemical analysis indicating a decrease in MgO concentration down the length of a boule, these findings suggest that the OH^- absorption peak shifting phenomenon is not a simple function solely of MgO concentration.

3.1.1 Ferroelectric poling

Ferroelectric poling of $LiNbO_3$ is normally accomplished by imposing an electric field along a crystal's polar z-axis while cooling it through its Curie transition. The poling operation can be incorporated into the Czochralski process itself or dealt with in a separate post-growth processing step. The effectiveness of a given set of poling conditions is most easily tested through standard techniques for $LiNbO_3$ domain decoration involving polishing, etching, and optical microscopy[8]. Undoped $LiNbO_3$ of the congruent composition has a Curie temperature of roughly 1140°C and a melting point of roughly 1250°C. Typical poling conditions involve a poling field of roughly 0.5 V/cm.

In the present work, poling was carried out in a separate, post-growth process. Actual poling experimentation was limited to the first two crystals grown. As shown in Table 3, Curie temperature values for the $MgO:LiNbO_3$ grown in this work ranged from 1205 to 1222°C. Given an $MgO:LiNbO_3$ melting point less than that for undoped $LiNbO_3$, the range of poling process starting temperature is comparatively limited.

Despite the consequent constraint of necessarily well-controlled temperature programming in the poling furnace, it was determined that, provided the entire boule was allowed sufficient time to reach a temperature throughout its volume in excess of its Curie temperature, the 0.5 V/cm poling field used for undoped $LiNbO_3$ was sufficient to pole the $MgO:LiNbO_3$ without attendant damage. Although a number of boules were checked using polishing/etching/microscopy for the effectiveness of the poling operation, there was no evidence of domain multiplicity either in these tests or in subsequent optical characterization of any of the crystals.

3.1.2 Photorefractive effect (PRE) testing

A number of the crystals were characterized for PRE susceptibility. Samples from Z-6, Z-8, Y-2, Y-3, and a standard undoped optical-grade $LiNbO_3$ boule were fabricated or re-fabricated into test specimens measuring 5.5x7x8mm (x × y × z). The x-faces were polished to typical optical surface specifications but not anti-reflection coated. The test set-up is shown in figure 22. An argon ion laser with 3.2W of cw operating power at 488nm was used in creating PRE damage in the specimens. Beam propagation was along x with polarization parallel to z. PRE damage was quantified through measurement of optical power passing through an aperture placed after the crystal in the optical path. For each specimen, PRE damage was measured versus time, temperature, and incident power.

Figure 23 illustrates the results. Each data point represents the normalized laser power passing through the aperture after reaching steady-state PRE conditions in a given sample. After a change in temperature or laser fluence, tens of seconds were typically required to reach such steady-state conditions. No hysteresis was detected on cycling the temperature or laser fluence, provided sufficient time was allowed to reach steady-state.

Several points are notable about the data in figure 23. First, for a given sample and a given fluence, thermal annealing of PRE is evident. Contrary to previous reports, however, the "annealing temperature" ensuring absence of PRE is clearly a function of both MgO concentration and fluence. Second, PRE in a given sample at a given temperature is a function of laser fluence. Although not surprising, this observation has

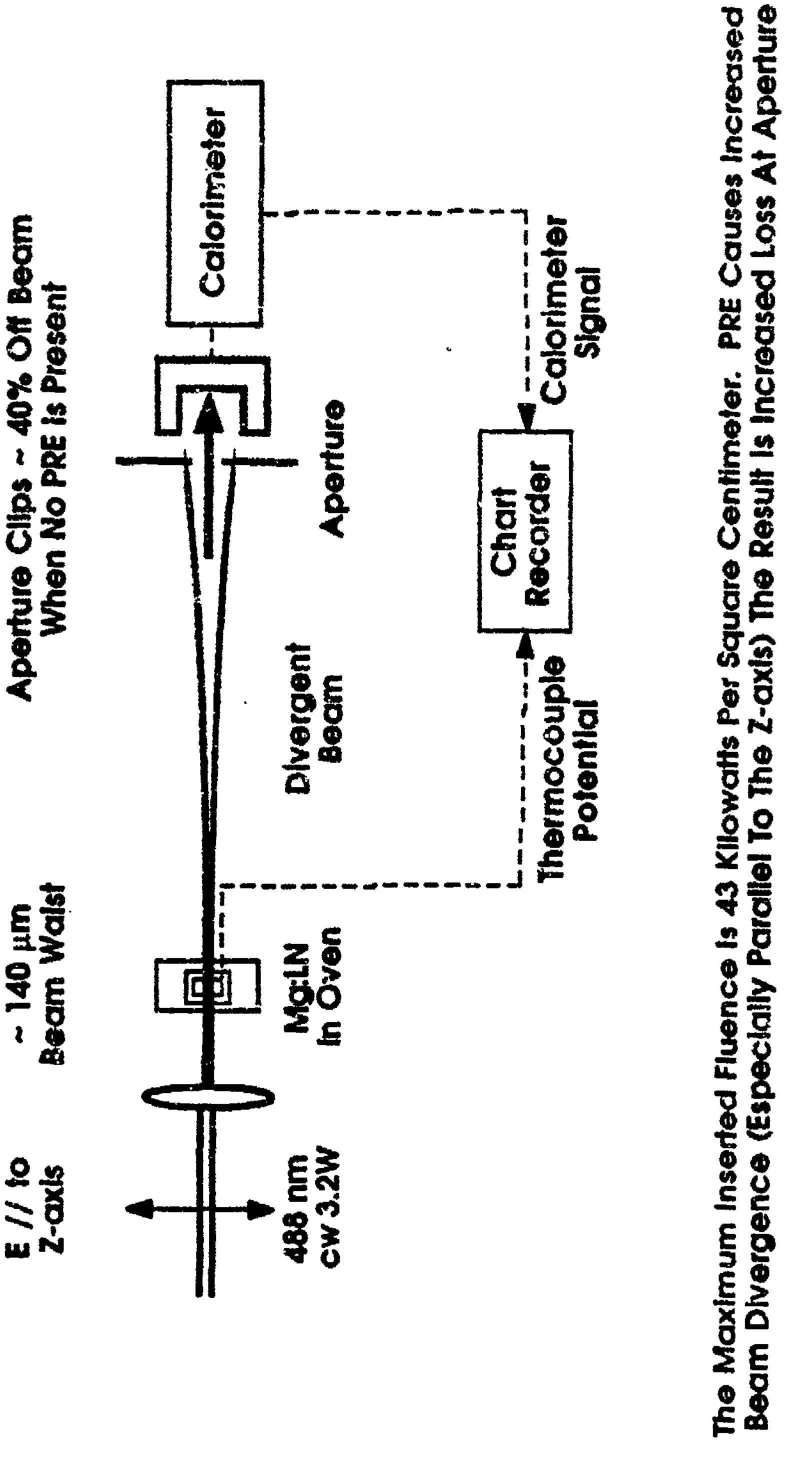

The Maximum Inserted Fluence Is 43 Kilowatts Per Square Centimeter. PRE Causes Increased Beam Divergence (Especially Parallel To The Z-axis) The Result Is Increased Loss At Aperture

Figure 22. *Photorefractive effect (PRE) testing.*

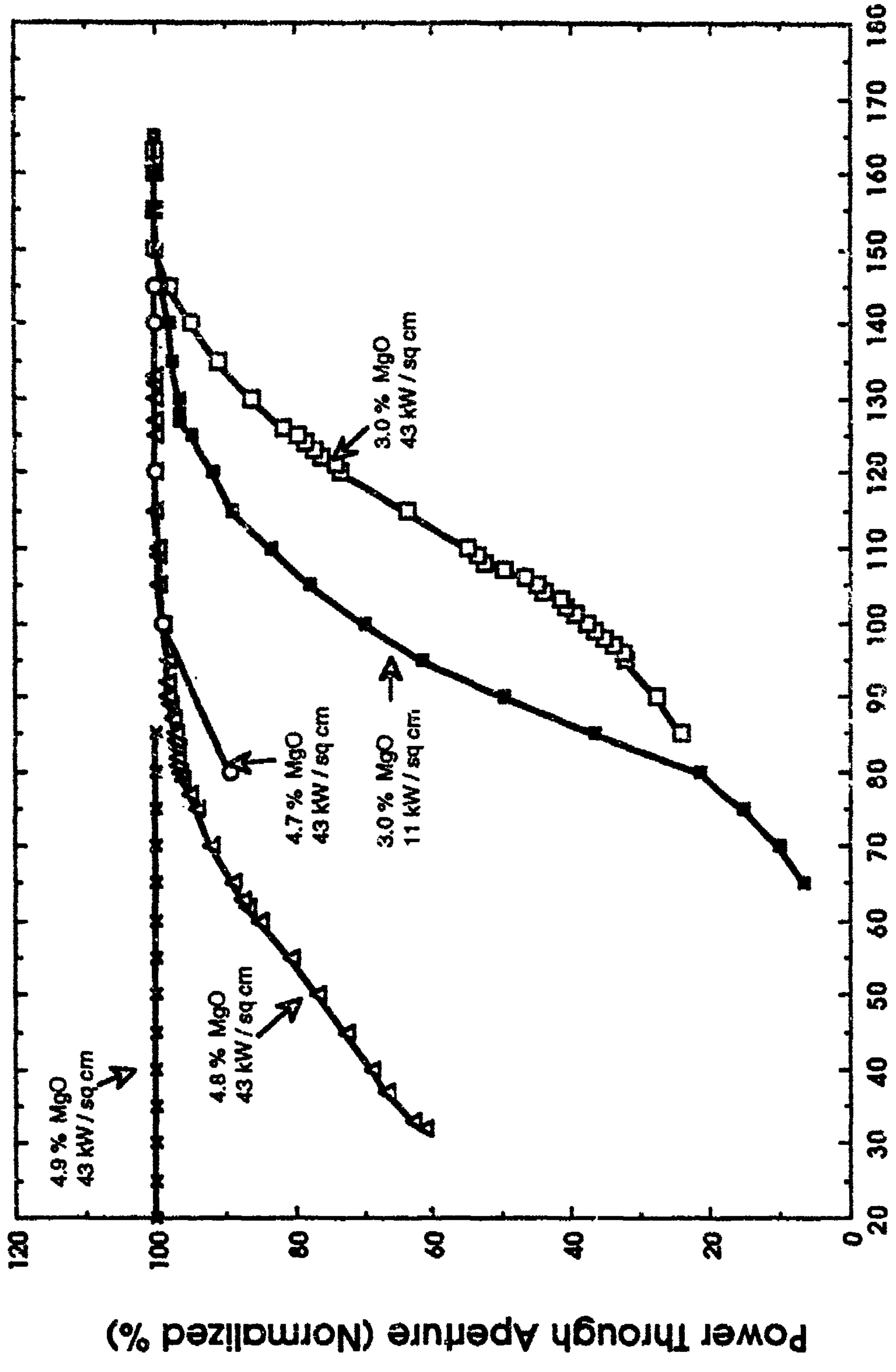

Figure 23. PRE in Mg:LiNbO$_3$ vs. temperature, [MgO] and beam intensity.

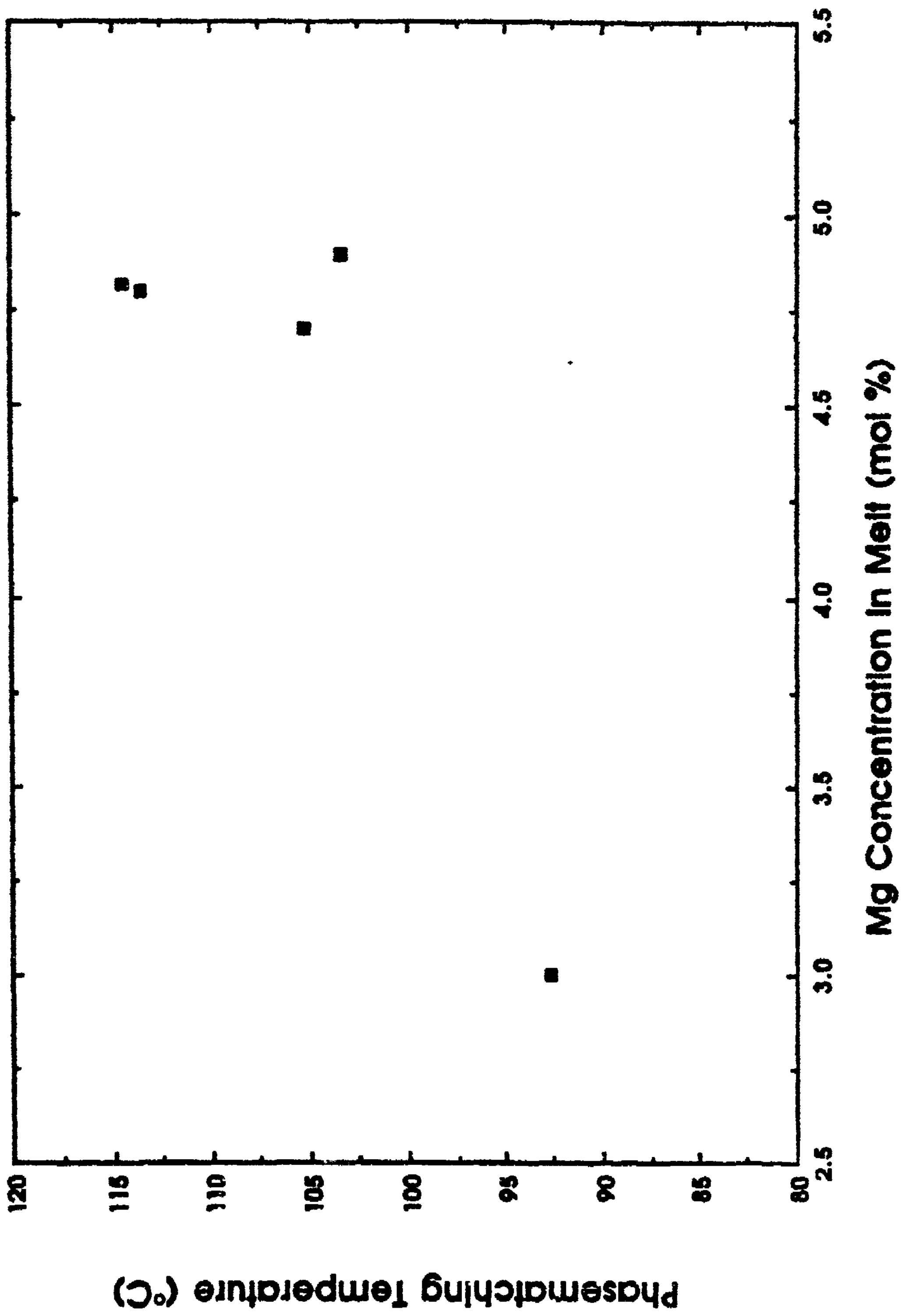

Figure 24. Phasematching temperature as a function of [MgO].

not been previously reported. Third, similar to Bryan's report [7], at a given temperature and fluence, PRE is clearly a function of MgO concentration for concentration values less than roughly 5 mol%. Although the data were left off figure 23, the test specimens fabricated from undoped $LiNbO_3$ were observed to allow minimum power through the aperture for a 43 kW/cm^2 fluence until the first onset of thermal annealing effects above 165°C. Fourth, for the one sample tested with a sufficiently high MgO concentration to exhibit a "shifted" IR absorption peak, it was impossible to induce measurable PRE for all tested conditions of fluence, exposure time, and temperature. The presumably most severe set of these conditions involved a fluence of 43 kW/cm^2 for 16 hours at 20°C.

3.1.3 NLO phase-matching measurements

Measurements were made of the temperature for non-critical phase-matching of second harmonic generation from a 1064 nm laser source. The subject crystals were the same as those characterized for PRE susceptibility and the test specimens were prepared to the same dimensions and specifications. A single longitudinal mode laser was Q-switched at 10 Hz to produce temporally smooth pulses of 11 ns duration. Propagation was along x with the 1064 nm fundamental polarized along z and the 532 nm second harmonic polarized along y. The fundamental and second harmonic were separated using a thin-film interference filter. Signal intensity at each wavelength was measured with fast silicon detectors. Sample temperature was controlled and ramped in cycles using a small oven and controller. Sample temperature was measured with a type-J thermocouple. Phase-matching temperature was determined as the ratio of 532 nm signal to 1064 nm reached its highest value in each temperature cycle.

The results are shown in figure 24. The dramatic peak in phase-matching temperature versus MgO concentration has not previously been reported. It is notable that the MgO concentration values in the region of the peak correspond to the discontinuous shift in the IR absorption peak for OH^-. A physical explanation for such behavior is not obvious, although similar peaks in the composition dependence of phase-matching temperature have recently been reported for vapor transport equilibrated $LiNbO_3$ crystals with solid compositions near 50 mol% Li_2O[9]. These off-congruent composition crystals were not tested for photorefractive effects.

3.2 DISCUSSION

In terms of macroscopic crystal quality, $MgO:LiNbO_3$ is clearly more difficult to grow than undoped $LiNbO_3$, and the difficulty increases with MgO concentration. For a given MgO concentration, growth along the crystallographic z-axis is easier than growth along the y-axis which is in turn easier than growth along the x-axis. Planar striae are present for all growth orientations. The striae, with a spacing of roughly 200 μm, run perpendicular to the growth direction and are visible with z-polarized light.

The ferroelectric poling conditions that were developed for $MgO:LiNbO_3$ based on standard poling conditions for undoped $LiNbO_3$ adjusted for the increased Curie temperature are effective and reproducible.

PRE damage threshold is a function of temperature and laser fluence. Both PRE damage threshold and NLO phase-matching temperature are functions of MgO concentration, particularly in the vicinity of 5 mol%. For one crystal doped with a high MgO concentration, it was impossible to induce measurable PRE damage for all tested conditions of laser power, exposure time, and temperature.

The discontinuous shift in the IR absorption peak associated with residual OH^- appears to be an important indicator of some dramatic optical property changes in $MgO:LiNbO_3$. The peak shift appears to be a function of several parameters including but not limited to MgO concentration.

Commercial NLO product development efforts are currently underway utilizing the PRE damage-resistant $MgO:LiNbO_3$ composition identified through this project. Of particular interest is resonant frequency doubling of a 1064 nm fundamental. Various waveguide-based NLO technologies are under development as well.

Additional research on $MgO:LiNbO_3$ is warranted to investigate several issues identified in this project. First, the relationships between crystal composition, point defect structures, and PRE mechanisms appear to be both theoretically complex and technologically significant. Second, the effect of MgO additions beyond the 5 mol% level remains largely unexplored. Third, if desirable from the standpoint of optical performance (even though scattering levels are low enough for present applications), the possibility exists for further reduction or even elimination of the observed planar striae through application of Czochralski process-control improvements currently under development for undoped $LiNbO_3$.

An issue not explored in this work concerns the influence of electric fields on PRE damage in $MgO:LiNbO_3$. A significant decrease in PRE damage threshold has been observed in some $MgO:LiNbO_3$ subjected to DC fields for purposes of piezoelectric locking to laser cavity resonances. A complete understanding of PRE in $MgO:LiNbO_3$ will have to account for such observations.

Finally, it should be mentioned that work is in progress doping $LiNbO_3$ with other species analogous to MgO[10]. Through this work, it is hoped to maintain the beneficial effects of PRE resistance while avoiding or reducing some of the processing-related deficiencies of $MgO:LiNbO_3$.

4 CONCLUSIONS

It appears from the present work that absorption losses are significantly higher than scattering losses in $MgO:LiNbO_3$, regardless of MgO concentration, as long as no catastrophic flaws (cracks) are visible. The likelihood of flaws increases with MgO concentration, although X-grown crystals are the most likely to present flaws, even with small amounts of MgO. The quality of Z-grown boules appeared more immune to [MgO], and Y-grown boules showed sensitivity to [MgO] between that of X- and Z-grown material.

The changes in formulation in the intrinsic crystal, where $[Li_2O]$ is changed between 48.60% to 48.38% appear to have no effect in absorption, or at least are drowned by variations observed in crystal quality. It appears then that this slight change in formulation will not affect other conclusions that can be drawn from the data.

The optimal results in scattering and absorption were obtained with Z-grown crystals, perhaps due to prior experience.

The most striking observation concerns the means of attaining low absorption: using Z-polarized light, whereas Z-propagation causes the most absorption. This should have important consequences for the applications as well as the choice of growth axis, depending on the total light path required.

Finally, the fact that large variations can be observed among different samples from the same boule points to the lack of uniformity found in this kind of crystal. In most cases, the variations within one boule are comparable to the differences among boule averages --both in scattering and absorption. In cases where the quality is critical, measuring attenuation in each crystal may be the only way to insure reliability.

APPENDIX A - THERMAL ANALYSIS

Consider light incident on a crystal, with incident power P_0. The injected power is then

$$P_1 = T P_0 \qquad (A1)$$

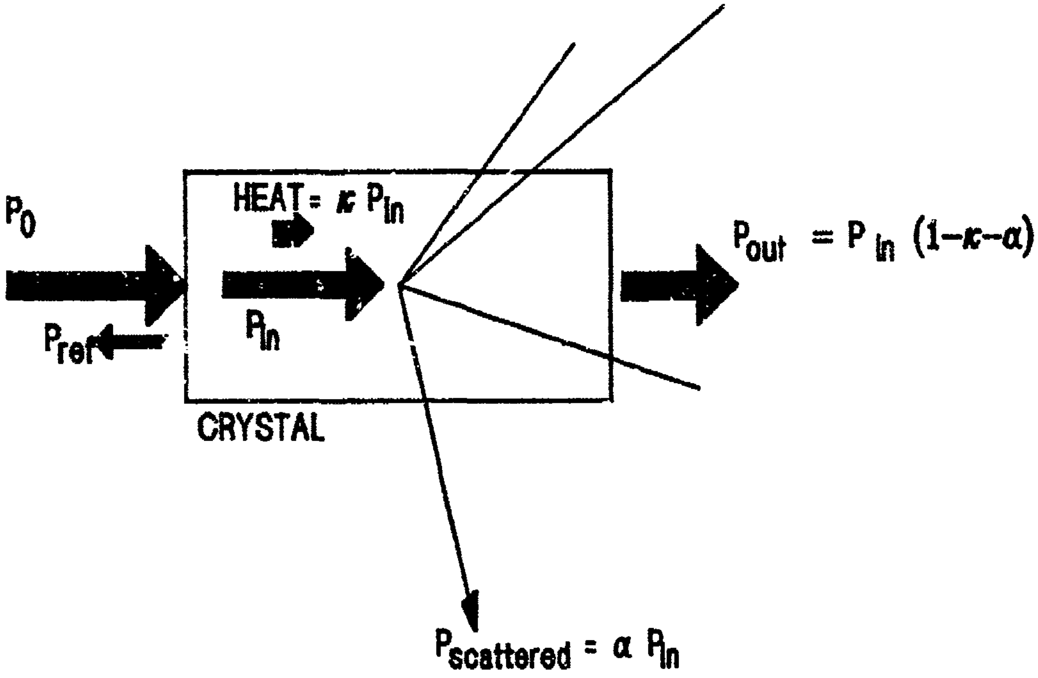

where $T = 1-R$ is the transmission coefficient across the surface, and the reflectivity is given by the index of refraction of the crystal, assuming normal incidence:

$$R = [(n - 1) / (n + 1)]^2 \qquad (A2)$$

after traveling through a length of crystal L, the absorbed power is

$$A_1 = T P_0 (1 - e^{-\lambda L}) \qquad (A3)$$

and upon reaching the other end of the crystal a fracti[illegible] the remaining power will be reflected back, yielding a second contribution to absorption:

$$A_2 = T P_0 e^{-\lambda L} R (1 - e^{-\lambda L}) \qquad (A4)$$

Adding all the contributions from internal reflections leads to a total absorbed power

$$A = A_0 + A_1 + \dots = \kappa P_0 \qquad (A5)$$

where κ is the absorbed fraction, and the absorption coefficient λ can be expressed in terms of κ, T and R by

$$\lambda = (1/L) \ln \{ (T - \kappa R)/(T - \kappa) \} \qquad (A6)$$

which in the $T \approx 1$, $R \approx 0$ approximation reduces to

$$\lambda = - (1/L) \ln (1 - \kappa) \qquad (A7)$$

Calorimetry

Now let us consider a body of mass m and heat capacity C_E. The temperature change dT/dt is given by its change in heat:

$$dq/dt = m\, C_E\, (dT/dt) \qquad (A8)$$

which is equal to the fraction κ of absorbed power P_0 minus the radiated power:

$$m\, C_E\, dT/dt = \kappa P_0 - \rho\, (T - T_0) \qquad (A9)$$

where ρ is a radiation coefficient accounting for radiative and conductive thermal losses, and T_0 is the ambient temperature. Changing variables to relative temperature, the equivalent of subtracting the ambient temperature as monitored by a neighboring thermistor,

$$y = T - T_0 \qquad (A10)$$

equation (9) above can be written as

$$dy/dt = a\, P_0 - r\, y \qquad (A11)$$

with an absorption term $a = \kappa / (m\, C_E)$ and a radiative term $r = \rho / (m\, C_E)$. If one heats the body, the absorption and radiative terms are present, yielding a time dependency (defining $y(0)=0$):

$$y(t) = P_0\, (a/r)\, (1 - e^{-r t}) \qquad (A12)$$

but during cooling only the radiative term is present, so if at $t'=0$ we define $y(t')=y_0$,

$$y(t') = y_0\, e^{-r\,t'} \tag{A13}$$

In other words, the term r can be obtained from the cooling off curve, and then used to determine the term a from the heating curve. The cooling off curve is first linearized and then fit to a straight line by a least squares algorithm: the slope determines r since

$$\ln\,(\, y(t')/y_0\,) = -\,r\,t' \tag{A14}$$

then the heating curve can be linearized and least-squares fit to obtain a:

$$y(t)\, r \,/\, P_0 = a\,(\,1 - e^{-r\,t}\,) \tag{A15}$$

This allows taking into account all data points, and a judicious sampling allows a reasonable weighing of the samples.

Thermistor mass corrections

To account for the contribution of the thermistor/epoxy mass m_t to the thermal mass of the crystal m_c, we can define the equivalent mass

$$m_{eq} = m_c + m_t \times (C_{Et}\, /\, C_{Ec})$$

where C_{Et} is the thermistor/epoxy heat capacity and C_{Ec} that of the crystal by itself. All the crystals were weighed before and after applying the thermistor, so m_t is known. C_{Et} was estimated at 10.6 (Cal/°-mol), the value for SiO_2, as recommended by the thermistor manufacturer.

APPENDIX B - FRESNEL EFFECTS

When a beam of light enters normal to the surface of a crystal whose exit surface is nearly parallel to the first one, a set of Fresnel reflections is established. Since for the case at hand the reflection coefficients are rather small, the interference pattern is of no concern.

Consider an incident beam with intensity I_0 striking a crystal of thickness d, whose interface has a reflectivity R (transmissivity T = 1 - R), as shown in figure B-1. The reflected beam intensity can be expressed as a series that adds up to

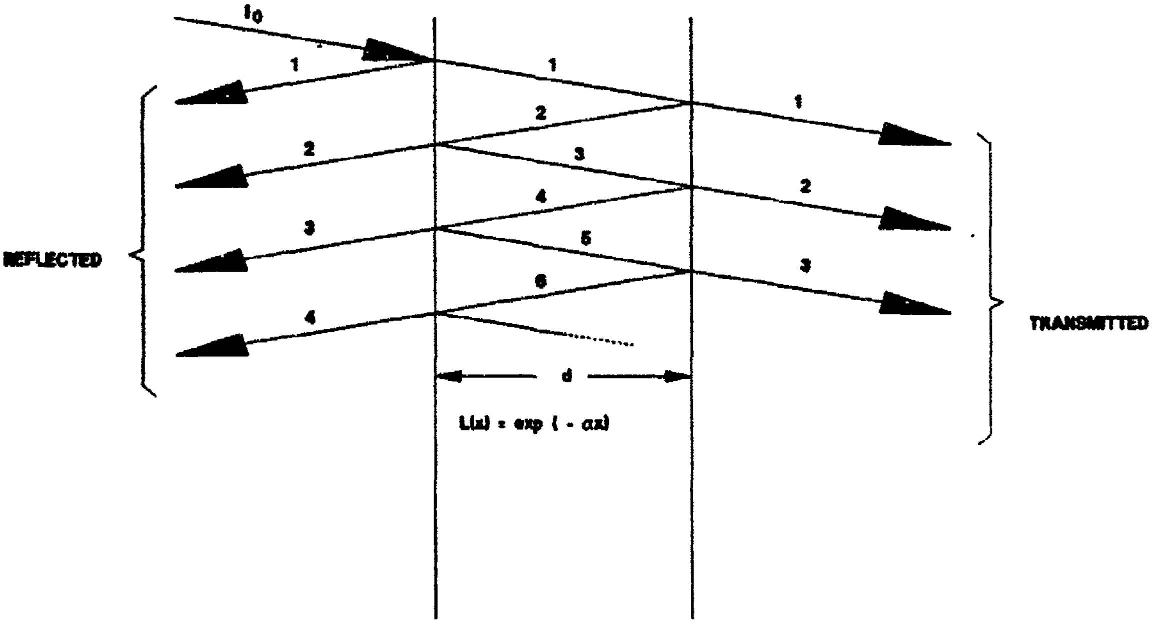

Figure B-1. Reflected beam series in a cell with parallel walls.

$$I_R = I_0 R \{ 1 + L^2 (1 - 2 R) \} / [1 - R^2L^2] \tag{B1}$$

where $$L = e^{-\lambda d} \tag{B2}$$

and λ is the total loss (absorption α and scattering σ):

$$\lambda = \alpha + \sigma \tag{B3}$$

Similarly, the transmitted intensity is a series that converges to

$$I_T = I_0 \, T^2 \, L \, / \, [1 - R^2 L^2] \tag{B4}$$

and the lost (absorbed or scattered) intensity (after infinite number of internal reflections) is

$$I_A = I_0 \, T \, (1 - L) \, / \, (1 - L R) \tag{B5}$$

which is the equivalent of equation A-6 in Appendix A.

Let us now look a the beam intensity as it zig-zags through the crystal. The remaining intensity after travelling a distance $l = n \, d + x$ is

$$I(l) = I_0 \, T \, R^n \, e^{-\lambda \, (nd+x)} \tag{B6}$$

that is, it exponentially decays along the material, suffering drastic losses at each reflection. This dependency is shown in figure B-2, for a rather lossy material ($\alpha = 0.5$) one inch thick.

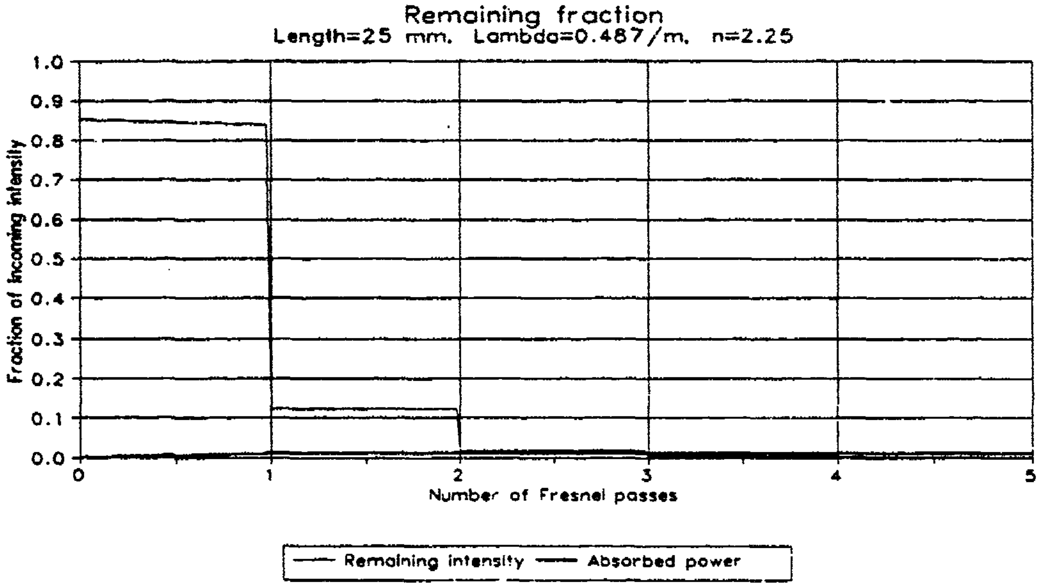

Figure B-2. Remaining beam intensity.

The fraction of the beam intensity that is absorbed at the interval between x and x+dx, (provided the interval does not contain a reflexion), is

$$I_a(l, l+dx) = I(l) \times \alpha \times dx \tag{B7}$$

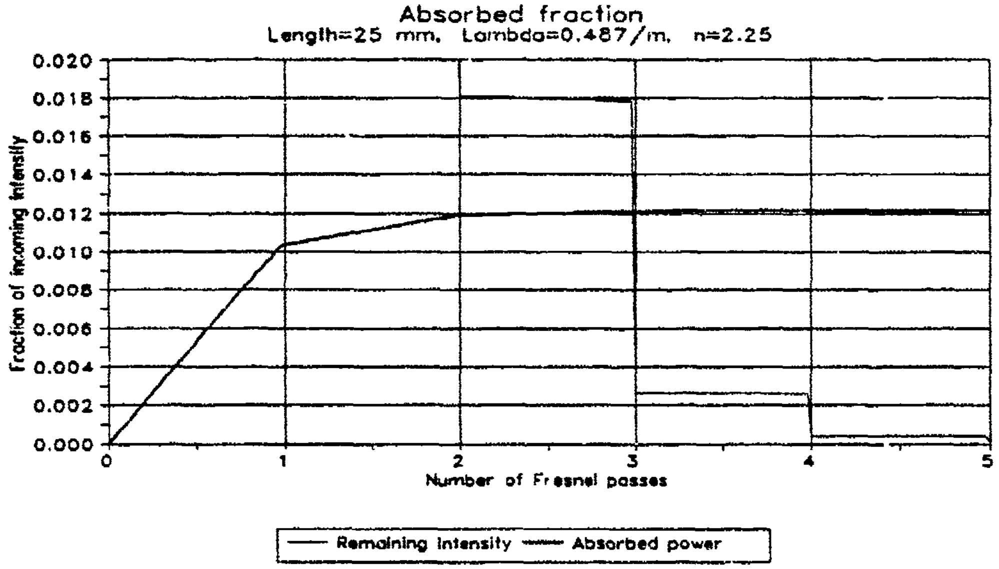

Figure B-3. Absorbed fraction.

Since I(l) is discontinuous, the integral is a rather un-elegant series. It was calculated for the same case described above, and it is shown in figure B-3. Note that figures B-2 and B-3 contain the same curves, differing only in the vertical scale.

Although the intensity of the beam decays rapidly within a few reflections, it remains large compared with the absorbed fraction: if the beam touches the walls generating absorption against non-transparent walls, even after four reflections, this contribution to the deposited power can cause significant measurement errors. This effect was an important consideration in performing the measurements outlined in the present report.

REFERENCES

1. Gi-Guo Zhong, Jin Jan, and Zhong-Kang Wu, in: Proc. 11th Intern. Quantum Electronics Conf., IEEE Cat. No. 80, CH 1561-0 June 1980, p. 631.
2. G. Magel & R. Byer, SPIE O-E/LASER '86 Conference Proceedings, paper 618-13, June, 1986.
3. J.S. Steinhart and S.R. Heart, Deep Sea Research 15, p. 497, (1968).
4. P.F. Bordui, R.G. Norwood, C.D. Bird, and G.D. Calvert, "Compositional Uniformity in Growth and Poling of Large-Diameter Lithium Niobate Crystals", J. Crystal Growth, 113 (1991) pp. 61-68.
5. P.F. Bordui, R.G. Norwood, and M.M. Fejer, Ferroelectrics 115, 7 (1991).
6. J.L. Nightingale, W.J. Silva, G.E. Reade, A. Rybicki, W.J. Kozlovsky, and R.L. Byer, Proc. S.P.I.E. 20, 681 (1986).
7. D.A. Bryan, R.R. Rice, R. Gerson, H.E. Tomaschke, K.L. Sweeney, and L.E. Halliburton, Opt. Eng. 24, 138 (1985).
8. A. Reüber, in Current Topics in Material Science, vol. 1, Ed. E. Kaldis (North-Holland, Amsterdam, 1978), pp. 481-601.
9. P.F. Bordui, R.G. Norwood, D.H. Jundt, and M.M. Fejer, "Preparation and Characterization of Off-Congruent Lithium Niobate Crystals", J. Appl. Phys. 71 No. 2 (1992).
10. T.R. Volk, V.I. Pryalkin, and N.M. Rubinina, Opt. Lett. 15 (1990) p. 996.

DISTRIBUTION LIST

No. of Copies — To

1 Office of the Under Secretary of Defense for Research and Engineering,
The Pentagon, Washington, DC 20301

Commander, U.S. Army Laboratory Command, 2800 Powder Mill Road, Adelphi,
MD 20783-1145
1 ATTN: AMSLC-IM-TL
1 AMSLC-CT

Commander, Defense Technical Information Center, Cameron Station, Building 5,
5010 Duke Street, Alexandria, VA 22304-6145
2 ATTN: DTIC-FDAC

1 MIAC/CINDAS, Purdue University, 2595 Yeager Road, West Lafayette, IN 47905

Commander, Army Research Office, P.O. Box 12211, Research Triangle Park,
NC 27709-2211
1 ATTN: Information Processing Office

Commander, U.S. Army Materiel Command, 5001 Eisenhower Avenue,
Alexandria, VA 22333
1 ATTN: AMCSCI

Commander, U.S. Army Materiel Systems Analysis Activity,
Aberdeen Proving Ground, MD 21005
1 ATTN: AMXSY-MP, H. Cohen

Commander, U.S. Army Missile Command, Redstone Scientific Information Center,
Redstone Arsenal, AL 35898-5241
1 ATTN: AMSMI-RD-CS-R/Doc
1 AMSMI-RLM

Commander, U.S. Army Missile Command, Redstone Arsenal, AL 35898-5253
1 ATTN: AMSMI-RD-AS-OG, Mr. Lee Pratt
1 AMSMI-RD, Mr. William Pittman

Commander, U.S. Army Missile Command, Redstone Arsenal, AL 35898-5270
1 ATTN: AMSMI-WS-PO, Dr. Don Gregory
1 AMSMI-WS-LS, Dr. Miles Holloman
1 AMSMI-WS-UB, Mr. William Friday

Director, U.S. Army Night Vision and Electro-optics Directorate, Ft. Belvoir,
VA 22060-0001
1 ATTN: AMSEL-NV-RD, Mr. David Caffey
1 AMSEL-NV-RD, Mr. Albert Pinto
1 AMSEL-NV-RD, Mr. Larry Merkle
1 AMSEL-NV-RD, Mr. Michael Ferry
1 AMSEL-NV-RD, Ms. Gerri Daunt
1 AMSEL-NV-RD, Larry Mizerka

Commander, U.S. Army Armament, Munitions and Chemical Command, Dover, NJ 07801
1 ATTN: Technical Library

Commander, U.S. Army Natick Research, Development and Engineering Center,
Natick, MA 01760-5010
1 ATTN: Technical Library

Commander, U.S. Army Satellite Communications Agency, Fort Monmouth, NJ 07703
1 ATTN: Technical Document Center

Commander, U.S. Army Tank-Automotive Command, Warren, MI 48397-5000
1 ATTN: AMSTA-ZSK
1 AMSTA-TSL, Technical Library

Commander, White Sands Missile Range, NM 88002
1 ATTN: STEWS-WS-VT

President, Airborne, Electronics and Special Warfare Board, Fort Bragg,
NC 28307
1 ATTN: Library

Director, U.S. Army Ballistic Research Laboratory, Aberdeen Proving Ground,
MD 21005
1 ATTN: SLCBR-TSB-S (STINFO)

Commander, Dugway Proving Ground, Dugway, UT 84022
1 ATTN: Technical Library, Technical Information Division

Commander, Harry Diamond Laboratories, 2800 Powder Mill Road, Adelphi, MD 20783
1 ATTN: Technical Information Office

No. of Copies	To
	Director, Benet Weapons Laboratory, LCWSL, USA AMCCOM, Watervliet, NY 12189
1	ATTN: AMSMC-LCB-TL
	Commander, U.S. Army Foreign Science and Technology Center, 220 7th Street, N.E., Charlottesville, VA 22901-5396
3	ATTN: AIFRTC, Applied Technologies Branch, Gerald Schlesinger
	Commander, U.S. Army Aeromedical Research Unit, P.O. Box 577, Fort Rucker, AL 36360
1	ATTN: Technical Library
	Commander, U.S. Army Aviation Systems Command, Aviation Research and Technology Activity, Aviation Applied Technology Directorate, Fort Eustis, VA 23604-5577
1	ATTN: SAVDL-E-MOS
	U.S. Army Aviation Training Library, Fort Rucker, AL 36360
1	ATTN: Building 5906-5907
	Commander, U.S. Army Agency for Aviation Safety, Fort Rucker, AL 36362
1	ATTN: Technical Library
	Commander, USACDC Air Defense Agency, Fort Bliss, TX 79916
1	ATTN: Technical Library
1	Clarke Engineer School Library, 3202 Nebraska Ave. North, Ft. Leonard Wood, MO 65473-5000
	Commander, U.S. Army Engineer Waterways Experiment Station, P. O. Box 631, Vicksburg, MS 39180
1	ATTN: Research Center Library
	Commandant, U.S. Army Quartermaster School, Fort Lee, VA 23801
1	ATTN: Quartermaster School Library
	Naval Research Laboratory, Washington, DC 20375
1	ATTN: Code 5830
1	Dr. G. R. Yoder - Code 6384
	Chief of Naval Research, Arlington, VA 22217
1	ATTN: Code 471
1	Edward J. Morrissey, WRDC/MLTE, Wright-Patterson Air Force, Base, OH 45433-6523
	Commander, U.S. Air Force Wright Research & Development Center, Wright-Patterson Air Force Base, OH 45433-6523
1	ATTN: WRDC/MLLP, M. Forney, Jr.
1	WRDC/MLBC, Mr. Stanley Schulman
	NASA - Marshall Space Flight Center, MSFC, AL 35812
1	ATTN: Mr. Paul Schuerer/EH01
	U.S. Department of Commerce, National Institute of Standards and Technology, Gaithersburg, MD 20899
1	ATTN: Stephen M. Hsu, Chief, Ceramics Division, Institute for Materials Science and Engineering
1	Librarian, Materials Sciences Corporation, 930 Harvest Drive, Suite 300, Blue Bell, PA 19422
1	The Charles Stark Draper Laboratory, 68 Albany Street, Cambridge, MA 02139
	General Dynamics, Convair Aerospace Division, P.O. Box 748, Fort Worth, TX 76101
1	ATTN: Mfg. Engineering Technical Library
1	Department of the Army, Aerostructures Directorate, MS-266, U.S. Army Aviation R&T Activity - AVSCOM, Langley Research Center, Hampton, VA 23665-5225
1	NASA - Langley Research Center, Hampton, VA 23665-5225
1	U.S. Army Propulsion Directorate, NASA Lewis Research Center, 2100 Brookpark Road, Cleveland, OH 44135-3191
1	NASA - Lewis Research Center, 2100 Brookpark Road, Cleveland, OH 44135-3191
1	Dr. Milan Kokta, Union Carbide, 750 S. 32nd St., Washougal, WA 98671
1	Mr. Gabe Loiacono, Crystal Associates, 15 Industrial Park, Waldwick, NJ 07463
1	Dr. Roger Belt, Allied Crystal Products, 200 E. Hanover St., Morris Plains, NJ 07950

No. of Copies	To
1	Professor John Gruber, Physics Department, 235 Old Science Bldg., San Jose State University, One Washington Square, San Jose, CA 95192
1	Dr. Fred Schmid, Crystal Systems, Inc., 35 Congress St., Salem, MA 01970
	Ginzton Laboratory, Stanford University, Stanford, CA 94605
1	ATTN: Dr. Marty Fejer
1	Dr. Robert Eckardt
1	Prof. Richard Shealy, Cornell Univ. Elec. Engrg. Dept., Ithaca, NY 14853-0001
1	Prof. C. L. Tang, Cornell Univ., 418 Phillips Hall, Ithaca, NY 14853-0001
	Deltronic Crystal Industries, Inc., 60 Harding Ave., Dover, NJ 07801
1	ATTN: Research Director
1	Somnath Sengupta, Res. Assoc., MIT, CMSE M/S 13-3153, 77 Massachusetts Ave., Cambridge, MA 02139-0001
	U.S. Army, 2800 Powder Mill Road, Adelphi, MD 20783-1145
1	ATTN: SLCHD-ST-AD, Dr. George Simonis
1	Prof. Sukant K. Tripathy, Univ. of Lowell, Dept. of Chemistry, Lowell, MA 01854-0001
1	Dr. Christine A. Wang, Res. Staff, MIT, M/S C-119, Lincoln Lab., 244 Wood St., Lexington, MA 02173-9108
1	Mr. T. (Mike) Wei, Res. Supr. GTE Labs., Inc., M/S 35, 40 Sylvan Road, Waltham, MA 02254-0001
1	Mr. Craig Willand, Eastman Kodak Co., Kodak Park, Rochester, NY 14650-2021
1	Mr. John J. Zola, VP, Crystal Assoc., 15 Industrial Park, Waldwick, NJ 07463-0001
1	Mr. Barry A. Wechsler, Mem. Tech. Staff, Hughes Res. Labs., M/S RL64, 3011 Malibu Canyon Road, Malibu, CA 90265-0001
1	Dr. John L. West, Assoc. Dir., Kent State Univ., Liquid Crystal Inst., Kent, OH 44242-0001
	U.S. Army, Natick RD&E Center, Kansas St., Natick, MA 01760-5020
1	ATTN: STRNC-YSP, Mr. Reginald A. Willingham
1	Pallab Bhattacharya, Univ. of Michigan, Dept. of Elec. Engrg., Computer Science, 1301 Beal Ave., Ann Arbor, MI 48109-2122
15	Mr. Peter F. Bordui, Crystal Dev. Mgr., Crystal Tech., Inc., 1040 E. Meadow Circle, Palo Alto, CA 94303-0001
1	Mr. Jeffrey H. Bohn, Staff Scientist, Cleveland Crystals, Inc., 676 Alpha Dr., Highland Hts., OH 44143
1	Dr. Lawrence H. Domash, Sr. Scientist, Foster-Miller, Inc., 350 Second Ave., Waltham, MA 02154-0001
1	Prof. Mildred Dresselhaus, MIT, Bldg. 13, Room 3005, Cambridge, MA 02139-4307
1	Dr. Mark A. Druy, Foster-Miller, Inc., 350 Second Ave. Waltham, MA 02254-0001
1	Mr. Albert Feldman, NIST, A329 Matls., Gaithersburg, MD 20399-0001
1	Dr. Arlete Cassanho, MIT Rm. 13-3146, 77 Massachusetts Ave., Cambridge, MA 02139-0001
1	Dr. Martin Drexhage, Galileo Electrooptics Corp., P.O. Box 550, Sturbridge, MA 01566-0001
1	Mr. Robert Feigelson, Stanford Univ., Ct. for Matls. Res., Stanford, CA 94305-4045
1	Dr. Ronald P. Gale, VP Photovoltaics, Kopin Corp., 695 Myles Standish Blvd., Taunton, MA 02780-0001
	U.S. Army, Labcom ET & DL, Ft. Monmouth, NJ 07703-0001
1	ATTN: SLCET-MP, Mr. Thomas P. Higgins, Elec. Engr.
1	Dr. Richard H. Hopkins, Electronic & Photo. Matls. Mgr., Westinghouse, 1310 Beulah Road, Pittsburgh, PA 15235-0001
	U.S. Air Force, Wright-Patterson AFB, OH 45433-6533
1	ATTN: WL/MLP, Mr. Gordon H. Griffith, Tech. Advisor
	U.S. Air Force, Wright-Patterson AFB, OH 45433-6533
1	ATTN: WL/MLPO, Mr. F. Kenneth Hopkins

No. of Copies	To
	U.S. Navy, China Lake, CA 93555-0001
1	ATTN: NWC Code 3854, Mr. Daniel C. Harris, Head, Optical & Elec. Matls. Br.
	U.S. Army, Elec. Tech. & Devices Lab., Ft. Monmouth, NJ 07703-0001
1	ATTN: SLCET-EJ, Mr. Kenneth A. Jones, Elec. Matls. Br. Chf.
	U.S. Air Force, Rowe Laboratory, Hanscom AFB, MA 02173-0001
1	ATTN: Dr. D. Bliss
1	Dr. John Larkin
	U.S. Army, Ft. Belvoir, VA 22060-0001
1	ATTN: AMSEL-NV-RD-IRT, Mr. Lawrence J. Mizerka, Elec. Engr.
	U.S. Navy, NWC Res. Dept., China Lake, CA 93555-0001
1	ATTN: Code 3858, Mr. Geoffrey A. Lindsay
1	Prof. David C. Look, Res., Wright State Univ., Univ. Res. Ctr., Dayton, OH 45435-0001
1	Prof. Subhash Mahajan, Carnegie Mellon Univ., 5000 Forbes Ave., Pittsburgh, PA 15213-0001
1	Prof. T. F. Morse, Brown Univ., Lab. for Lightwave Tech. Div. of Engrg. Providence, RI 02912-0001
1	Mr. Richard W. Pekala, Polymer Sxn. Ldr., Lawrence Livermore Natl. Lab., M/S L-322, 7000 East Ave., Livermore, CA 94550-0001
	U.S. Army, P.O. Box 12211, Research Triangle Park, NC 27709-2211
1	ATTN: SLCRO, Dr. John T. Prater, Matls. Engr.
1	Mr. Axel Scherer, Bellcore, M/S NVC3X173, 331 Newmann Springs Rd., Red Bank, NJ 07701-0001
1	Mr. Peter G. Schunemann, Lockheed Sanders, Inc., MER 15-1813, P.O. Box 868, Nashua, NH 03061-0868
1	Prof. Richard M. Osgood, Jr., Columbia Univ. , Dept. of Elec. Engrg., 500 W 120th St., Mudd Bldg., New York, NY 10027-0001
	U.S. Army, 2800 Powder Mill Rd., Adelphi, MD 20783-1197
1	ATTN: SLCHD-ST-OP, Mr. John M. Pellegrino, Chf. Optical Proc. Tech.
1	Dr. Daniel Ryder, Tufts Univ., 4 Colby Street, Medford, MA 02156-0001
10	Dr. Richard Schlecht, LaserGenics, Inc., 2362 Qume Drive,Suite E, San Jose, CA 95131
1	Dr. P. Chandra Sekhar, Electrochemical Prog. Mgr., Gumbs Assoc., Inc., 11 Harts Ln., East Brunswick, NJ 08816-0001
	Director, U.S. Army Materials Technology Laboratory, Watertown, MA 02172-0001
2	ATTN: SLCMT-TML
1	SLCMT-IMA-V
1	SLCMT-PR
52	SLCMT-EMC, William A. Spurgeon (COR)

U.S. Army Materials Technology Laboratory
Watertown, Massachusetts 02172-0001
SINGLE CRYSTAL GROWTH OPTIMIZATION OF
MAGNESIUM-DOPED LITHIUM NIOBATE -
R. G. Schlecht, C. I. Zanelli, and A. M. Schlecht
LaserGenics Corporation, San Jose, California, and
P. F. Bordui, C. D. Bird, and R. Blackman
Crystal Technology, Inc., Palo Alto, California
Technical Report MTL TR 92-24, April 1992, 45 pp -
illus-tables, Contract DAAL04-88-C-0029
Final Report, Sep 88 to Dec 91

AD________________
UNCLASSIFIED
UNLIMITED DISTRIBUTION

Key Words

Lithium niobate (doped)
Crystal growth
Optical properties

The purpose of the Phase II program entitled "Single Crystal Growth Optimization of Magnesium-Doped Lithium Niobate" was to optimize the growth of $MgO:LiNbO_3$. The first step in this direction consisted of developing means and methods to accurately measure absorption losses (scattering loss methods were previously developed under a Phase I contract). It was known at the outset that very sensitive instrumentation would be required to allow measurements on small samples. The results of the measurements of both types of photon loss would then be used to optimize the molar concentration of MgO in $LiNbO_3$ to achieve crystals with low loss as well as high photorefractive damage threshold. Highly sensitive scattering and absorption facilities were developed and used in the process of optimizing crystal growth. The ability to accurately and routinely measure these parameters has allowed us to understand variability in the growth process, determine growth parameters, and --most importantly-- to observe that specific propagation and polarization directions are significantly less lossy than others. Studies were performed on the growth, poling, and resulting properties of MgO-doped lithium niobate. Both photorefractive damage threshold and NLO phase-matching temperature were observed to vary with MgO concentration. For one crystal doped with a high MgO concentration, it was impossible to induce measurable photorefractive damage.

U.S. Army Materials Technology Laboratory
Watertown, Massachusetts 02172-0001
SINGLE CRYSTAL GROWTH OPTIMIZATION OF
MAGNESIUM-DOPED LITHIUM NIOBATE -
R. G. Schlecht, C. I. Zanelli, and A. M. Schlecht
LaserGenics Corporation, San Jose, California, and
P. F. Bordui, C. D. Bird, and R. Blackman
Crystal Technology, Inc., Palo Alto, California
Technical Report MTL TR 92-24, April 1992, 45 pp -
illus-tables, Contract DAAL04-88-C-0029
Final Report, Sep 88 to Dec 91

AD________________
UNCLASSIFIED
UNLIMITED DISTRIBUTION

Key Words

Lithium niobate (doped)
Crystal growth
Optical properties

The purpose of the Phase II program entitled "Single Crystal Growth Optimization of Magnesium-Doped Lithium Niobate" was to optimize the growth of $MgO:LiNbO_3$. The first step in this direction consisted of developing means and methods to accurately measure absorption losses (scattering loss methods were previously developed under a Phase I contract). It was known at the outset that very sensitive instrumentation would be required to allow measurements on small samples. The results of the measurements of both types of photon loss would then be used to optimize the molar concentration of MgO in $LiNbO_3$ to achieve crystals with low loss as well as high photorefractive damage threshold. Highly sensitive scattering and absorption facilities were developed and used in the process of optimizing crystal growth. The ability to accurately and routinely measure these parameters has allowed us to understand variability in the growth process, determine growth parameters, and --most importantly-- to observe that specific propagation and polarization directions are significantly less lossy than others. Studies were performed on the growth, poling, and resulting properties of MgO-doped lithium niobate. Both photorefractive damage threshold and NLO phase-matching temperature were observed to vary with MgO concentration. For one crystal doped with a high MgO concentration, it was impossible to induce measurable photorefractive damage.

U.S. Army Materials Technology Laboratory
Watertown, Massachusetts 02172-0001
SINGLE CRYSTAL GROWTH OPTIMIZATION OF
MAGNESIUM-DOPED LITHIUM NIOBATE -
R. G. Schlecht, C. I. Zanelli, and A. M. Schlecht
LaserGenics Corporation, San Jose, California, and
P. F. Bordui, C. D. Bird, and R. Blackman
Crystal Technology, Inc., Palo Alto, California
Technical Report MTL TR 92-24, April 1992, 45 pp -
illus-tables, Contract DAAL04-88-C-0029
Final Report, Sep 88 to Dec 91

AD________________
UNCLASSIFIED
UNLIMITED DISTRIBUTION

Key Words

Lithium niobate (doped)
Crystal growth
Optical properties

The purpose of the Phase II program entitled "Single Crystal Growth Optimization of Magnesium-Doped Lithium Niobate" was to optimize the growth of $MgO:LiNbO_3$. The first step in this direction consisted of developing means and methods to accurately measure absorption losses (scattering loss methods were previously developed under a Phase I contract). It was known at the outset that very sensitive instrumentation would be required to allow measurements on small samples. The results of the measurements of both types of photon loss would then be used to optimize the molar concentration of MgO in $LiNbO_3$ to achieve crystals with low loss as well as high photorefractive damage threshold. Highly sensitive scattering and absorption facilities were developed and used in the process of optimizing crystal growth. The ability to accurately and routinely measure these parameters has allowed us to understand variability in the growth process, determine growth parameters, and --most importantly-- to observe that specific propagation and polarization directions are significantly less lossy than others. Studies were performed on the growth, poling, and resulting properties of MgO-doped lithium niobate. Both photorefractive damage threshold and NLO phase-matching temperature were observed to vary with MgO concentration. For one crystal doped with a high MgO concentration, it was impossible to induce measurable photorefractive damage.

U.S. Army Materials Technology Laboratory
Watertown, Massachusetts 02172-0001
SINGLE CRYSTAL GROWTH OPTIMIZATION OF
MAGNESIUM-DOPED LITHIUM NIOBATE -
R. G. Schlecht, C. I. Zanelli, and A. M. Schlecht
LaserGenics Corporation, San Jose, California, and
P. F. Bordui, C. D. Bird, and R. Blackman
Crystal Technology, Inc., Palo Alto, California
Technical Report MTL TR 92-24, April 1992, 45 pp -
illus-tables, Contract DAAL04-88-C-0029
Final Report, Sep 88 to Dec 91

AD________________
UNCLASSIFIED
UNLIMITED DISTRIBUTION

Key Words

Lithium niobate (doped)
Crystal growth
Optical properties

The purpose of the Phase II program entitled "Single Crystal Growth Optimization of Magnesium-Doped Lithium Niobate" was to optimize the growth of $MgO:LiNbO_3$. The first step in this direction consisted of developing means and methods to accurately measure absorption losses (scattering loss methods were previously developed under a Phase I contract). It was known at the outset that very sensitive instrumentation would be required to allow measurements on small samples. The results of the measurements of both types of photon loss would then be used to optimize the molar concentration of MgO in $LiNbO_3$ to achieve crystals with low loss as well as high photorefractive damage threshold. Highly sensitive scattering and absorption facilities were developed and used in the process of optimizing crystal growth. The ability to accurately and routinely measure these parameters has allowed us to understand variability in the growth process, determine growth parameters, and --most importantly-- to observe that specific propagation and polarization directions are significantly less lossy than others. Studies were performed on the growth, poling, and resulting properties of MgO-doped lithium niobate. Both photorefractive damage threshold and NLO phase-matching temperature were observed to vary with MgO concentration. For one crystal doped with a high MgO concentration, it was impossible to induce measurable photorefractive damage.